

1 **Quantifying the spatial-seasonal patterns of land-atmosphere water, heat and**  
2 **CO<sub>2</sub> flux exchange over the Tibetan Plateau from an observational perspective**

3 Binbin Wang<sup>1,2,5,6,7</sup>, Yaoming Ma<sup>1,2,3,4,5,6,7\*</sup>, Zeyong Hu<sup>8</sup>, Xuan Li<sup>1</sup>, Weiqiang Ma<sup>1,2,</sup>  
4 <sup>4,5,6,7</sup>, Xuelong Chen<sup>1,2,5,6,7</sup>, Cunbo Han<sup>1,2,5,6,7</sup>, Zhipeng Xie<sup>1,2,5,6,7</sup>, Yuyang Wang<sup>9</sup>,  
5 Maoshan Li<sup>10</sup>, Bin Ma<sup>1,5,6,7</sup>, Xingdong Shi<sup>1,4</sup>, Weimo Li<sup>1,4</sup>, Zhengling Cai<sup>1,4</sup>

6 <sup>1</sup>State Key Laboratory of Tibetan Plateau Earth System, Resources and Environment (TPESRE),  
7 Institute of Tibetan Plateau Research, Chinese Academy of Sciences, Beijing 100101, China;

8 <sup>2</sup>College of Earth and Planetary Sciences, University of Chinese Academy of Sciences, Beijing  
9 100049, China;

10 <sup>3</sup>College of Hydraulic & Environmental Engineering, China Three Gorges University, Yichang  
11 443002, China;

12 <sup>4</sup>College of Atmospheric Science, Lanzhou University, Lanzhou 730000, China;

13 <sup>5</sup>National Observation and Research Station for Qomolangma Special Atmospheric Processes and  
14 Environmental Changes, Dingri 858200, China;

15 <sup>6</sup>Kathmandu Center of Research and Education, Chinese Academy of Sciences, Beijing 100101,  
16 China;

17 <sup>7</sup>China-Pakistan Joint Research Center on Earth Sciences, Chinese Academy of Sciences, Islamabad  
18 45320, Pakistan;

19 <sup>8</sup>Key Laboratory of Land Surface Process and Climate Change in Cold and Arid Regions, Northwest  
20 Institute of Eco-Environment and Resources, Chinese Academy of Sciences, Lanzhou, 730000,  
21 China;

22 <sup>9</sup>College of Grassland Science and Technology, China Agricultural University, Beijing,  
23 100193,China;

24 <sup>10</sup>School of Atmospheric Sciences, Chengdu University of Information Technology, Chengdu  
25 610225, China;

26 Corresponding authors: Binbin Wang ([wangbinbin@itpcas.ac.cn](mailto:wangbinbin@itpcas.ac.cn)); Yaoming Ma ([yyma@itpcas.ac.cn](mailto:yyma@itpcas.ac.cn));  
27 Address: Building 3, Courtyard 16, Liucui Road, Chaoyang District, Beijing City, China. Zip code:  
28 100101.

36 **Abstract**

37 Land-atmosphere (LA) interactions, through the turbulent exchange of water, heat and CO<sub>2</sub> fluxes,  
38 strongly influence regional micro-climates, water cycles, energy budgets, and ecosystem dynamics. The  
39 Tibetan Plateau (TP), characterized by its vast extent, high elevation, strong solar radiation and extreme  
40 weather variability, remains underexplored due to the scarcity of LA observation sites, particularly in its  
41 western and northern regions. This study introduces a newly established research and observation  
42 platform, comprising 16 planetary boundary layer towers that span diverse landscapes and dynamic  
43 meteorological conditions. Across these sites, mean annual air temperature, wind speed, and liquid  
44 precipitation range from -3.5 to 18.5°C, 0.6 to 5.6 m s<sup>-1</sup>, and 43 to 2164 mm, respectively. Elevation  
45 exhibits significant correlations with all meteorological variables, highlighting the pronounced spatial  
46 heterogeneity of land-atmosphere coupling across the region. The turbulent fluxes of water and heat  
47 exhibit distinct seasonal patterns, with maximum sensible heat flux (*SH*) in April-May and latent heat  
48 flux (*LE*) in July-August. Most stations act as carbon sinks, with net ecosystem exchange (*NEE*; the net  
49 CO<sub>2</sub> exchange between the ecosystem and the atmosphere, where negative values indicate net ecosystem  
50 CO<sub>2</sub> uptake) ranging from -3.2 to -174.3 g C m<sup>-2</sup> a<sup>-1</sup>, except the Medog station, which behaves as a carbon  
51 source likely linked to vegetation disturbance and human activity. *LE* is significantly correlated with *SH*,  
52 *NEE* and ecosystem respiration, revealing a strong coupling among water, heat and carbon fluxes. This  
53 high-resolution, quality-controlled dataset provides critical in situ observations for studying water-heat-  
54 carbon coupling, validating models and satellite algorithms, and improving understanding of climate-  
55 ecosystem interactions over the TP. The whole datasets are freely available at the National Tibetan  
56 Plateau Data Center ( <https://doi.org/10.11888/Atmos.tpdc.302428>; Wang and Ma, 2025).

57 **Key words:** Land-atmosphere turbulent fluxes, spatial-temporal variations, comprehensive  
58 observation and research platform, Tibetan Plateau

59  
60  
61  
62  
63  
64  
65  
66  
67  
68  
69  
70  
71  
72  
73  
74  
75  
76

# 77 1 Introduction

78 Land-atmosphere (LA) interactions, which govern the flux exchanges of energy, water, and CO<sub>2</sub>  
79 between the Earth's surface and the atmosphere, are pivotal in shaping regional water cycles, climate  
80 dynamics, and ecosystem changes (Gentine et al., 2019; Ma et al., 2023; Santanello et al., 2018; Seo and  
81 Ha, 2022; Zhang et al., 2024). Thermal contrasts between distinct landforms—such as land vs. water,  
82 mountain vs. valley, and ocean vs. land — drive regional circulations like lake-land and mountain-valley  
83 breezes, as well as large-scale atmospheric motions, including monsoons (Gerken et al., 2014; Wu and  
84 Zhang, 1998; Wu et al., 2023). These LA interactions modulate a wide range of processes, including the  
85 dispersion of air pollutants, the transport of atmospheric moisture, the redistribution of clouds and  
86 precipitation, and the regulation of ecosystem carbon balance (Bei et al., 2018; Friedlingstein et al., 2022;  
87 Suni et al., 2015; Zhu et al., 2017). For instance, enhanced coupling between soil moisture and land  
88 surface temperature can intensify droughts and heatwaves in northern East Asia (Seo and Ha, 2022),  
89 where soil moisture deficits reduce evapotranspiration (*ET*), amplifying heatwave conditions,  
90 particularly in areas with sparse vegetation. Nonlinear feedbacks between *ET* and cloud formation remain  
91 poorly constrained in transitional zones between energy- and water-limited regimes (Zhang et al. 2024).  
92 Under global warming, LA interactions governing permafrost thaw, vegetation productivity, and  
93 ecosystem respiration play an increasingly important role in determining regional and global carbon  
94 budgets, especially over the data scarce regions (Turetsky et al., 2020; Wang et al., 2023b; Wei et al.,  
95 2021). Quantifying these coupled fluxes through in situ observations is thus essential for understanding  
96 Earth system responses to climate change.

97 Understanding LA interactions through coordinated, multidisciplinary, and multi-scale observations  
98 is crucial for addressing global challenges such as water resource management, land-use planning,  
99 climate change, and ecosystem preservation. In this context, key global initiatives—such as the First  
100 International Satellite Land Surface Climatology Project Field Experiment (United States) (Sellers et al.,  
101 1992), the Hydrologic Atmospheric Pilot Experiment (France, Niger) (André et al., 1986; Goutorbe et  
102 al., 1997), the Northern Hemisphere Climate Processes Land Surface Experiment (Sweden) (Halldin et  
103 al., 1999), the Boreal Ecosystem–Atmosphere Study (Canada) (Sellers et al., 1995), the Inner Mongolia  
104 Semiarid Grassland Soil–Vegetation–Atmosphere Interaction and the Heihe River Basin Field  
105 Experiment (China) (Liu et al., 2018; Lü et al., 1997)—have provided foundational insights into LA  
106 interactions and have advanced parameterizations for climate models. Tibetan Plateau (TP), one of the  
107 world's most climate-sensitive and data-scarce region, plays a particularly critical role in the climate and  
108 ecology dynamics. TP exerts remarkable influence on atmospheric processes, generating thermal  
109 disturbances that affect circulation patterns, weather, and climate not only in China and East Asia but  
110 also globally (Wu and Zhang, 1998; Ye and Wu, 1998). For example, mesoscale system vortices and  
111 shear lines created in the TP's atmospheric boundary layer can lead to extreme weather events, such as  
112 heavy rain and storms, impacting both the plateau and surrounding regions (Li et al., 2020; Xu and Chen,  
113 2006). Thus, LA coupling and dynamics are important for the formation and development of weather  
114 systems. Over the past few decades, large-scale field activities and long-term observational  
115 experiments—such as Qinghai-Xizang Plateau Meteorology Experiment (QXPME), the Tibetan  
116 Plateau Atmospheric Scientific Experiment II and III (TIPEX-II, TIPEX-III), the Sino Japanese inter  
117 governmental cooperation project (JICA), the Global Energy and Water Cycle Experiment Asian  
118 Monsoon Experiment on the Tibetan Plateau (GAME/Tibet), the Coordinated Enhanced Observing  
119 Period (CEOP) Asia-Australia Monsoon Project on the Tibetan Plateau (CAMP/Tibet), etc. —have

120 greatly enhanced our understanding of land surface processes in the TP (Huang et al., 2023; Ma et al.,  
121 2023), and these efforts have also helped refine climate model parameterization, improving our ability  
122 to predict TP's climatic effects. However, the stations for measuring heat, water and CO<sub>2</sub> fluxes are  
123 concentrated mostly in the east and still rarely distributed over the vast northern and western regions,  
124 hindering our understanding on its spatial distribution and total amounts of heat, water and CO<sub>2</sub> flux.  
125 Given the growing challenges posed by global climate change, accurately measuring and modeling LA  
126 interaction processes is more critical than ever, and such efforts are essential for predicting climate  
127 extremes, managing water resources, and supporting sustainable ecology (Sun et al., 2015).

128 Although several LA interaction studies have analyzed seasonal variations in turbulent fluxes and  
129 their controlling factors (Ma et al., 2005; Ma et al., 2018; Ma et al., 2023; Wang et al., 2011; Yang et al.,  
130 2008), the lack of spatially distributed eddy-covariance (EC) sites has resulted in large uncertainties in  
131 flux estimates and interannual variability, especially over underrepresented ecosystem types over the  
132 western and northern TP. Previous modeling and remote-sensing efforts have improved regional *ET*  
133 estimates, yet still rely on limited ground validation measurements (Ma and Zhang, 2022; Yuan et al.,  
134 2024). For example, the water-carbon coupled biophysical model (Ma and Zhang, 2022) and an improved  
135 *ET* model (Yuan et al., 2021) are validated with EC measurements, both yielding annual *ET* value of  
136 approximately 350 mm yr<sup>-1</sup>. However, factors influencing the inter-annual variations in *ET* exhibit large  
137 biases and uncertainties, especially for data-scarce western and northern regions. As for carbon function,  
138 TP contains extensive permafrost and a variety of landscapes, including alpine meadows, alpine steppes,  
139 alpine shrubs, alpine wetlands, forests, and alpine deserts, which have a substantial impact on the carbon  
140 sink/source function of the region, and shows important ecological and environmental consequences.  
141 Recent studies indicate that most alpine meadows on the TP function as carbon sinks, with values ranging  
142 from -430 to -12.5 g C m<sup>-2</sup> a<sup>-1</sup>, and some alpine steppe areas act as weak carbon sources (Wang et al.,  
143 2023a; Wei et al., 2021). Specifically, alpine grasslands exhibit a weaker carbon sink function, with  
144 values ranging from -206.9 to -17.1 g C m<sup>-2</sup> a<sup>-1</sup> whilst shrub lands show even lower carbon sink values,  
145 ranging from -89.5 to -40.7 g C m<sup>-2</sup> a<sup>-1</sup> (Wei et al., 2021). Marshes display considerable variability in  
146 carbon fluxes, with values ranging from -187 ± 29 g C m<sup>-2</sup> a<sup>-1</sup> in Shenzha to -478 g C m<sup>-2</sup> a<sup>-1</sup> in Haibei  
147 (Qi et al., 2021; Zhao et al., 2005). Therefore, by synthesizing EC and climate data from multiple sites  
148 across the TP, we can clearly understand the spatial and temporal variations of water, heat, CO<sub>2</sub> fluxes  
149 and identify the mechanisms that control them.

150 To address these knowledge gaps, this study introduces a comprehensive multi-site observation  
151 network for monitoring LA exchanges of water, heat, and CO<sub>2</sub> fluxes across the TP (Fig. 1 and Table 1).  
152 The dataset encompasses 16 stations strategically distributed along major hydrothermal and ecological  
153 gradients, including alpine meadow, steppe, shrubland, and forest ecosystems. These standardized, long-  
154 term EC observations provide unprecedented spatial coverage, particularly over the data-scarce western  
155 and northern TP. The network offers a unique opportunity to investigate (1) What are the characteristics  
156 of land-atmosphere water, heat, and CO<sub>2</sub> fluxes across different landscapes of the TP? (2) What are the  
157 spatial and temporal distributions of water, heat, and CO<sub>2</sub> fluxes, and what factors influence these  
158 variations? This paper introduces the design and implementation of the observation platform, instrument  
159 configuration, and standardized data processing methods, followed by an analysis of the spatial-temporal  
160 variations of meteorological conditions, energy components, and CO<sub>2</sub> fluxes. Specifically, Sect. 3.1  
161 describes the spatial-temporal patterns of atmospheric meteorological variables such as air temperature,  
162 humidity and wind speed. Sect. 3.2 focuses on liquid precipitation and soil water content, which jointly

163 reflect regional water availability. Sect. 3.3 examines the energy flux components (sensible and latent  
164 heat fluxes, etc.), highlighting differences between wet and dry conditions and Sect. 3.4 analyzes the  
165 seasonal variations of carbon fluxes (net ecosystem exchange (*NEE*), gross primary productivity (*GPP*)  
166 and ecosystem respiration (*Re*)). By making this dataset publicly available, we aim to fill a critical gap  
167 in global flux observations and provide a foundation for advancing land–atmosphere interaction research,  
168 model evaluation, and climate prediction over high-elevation ecosystems of the TP.

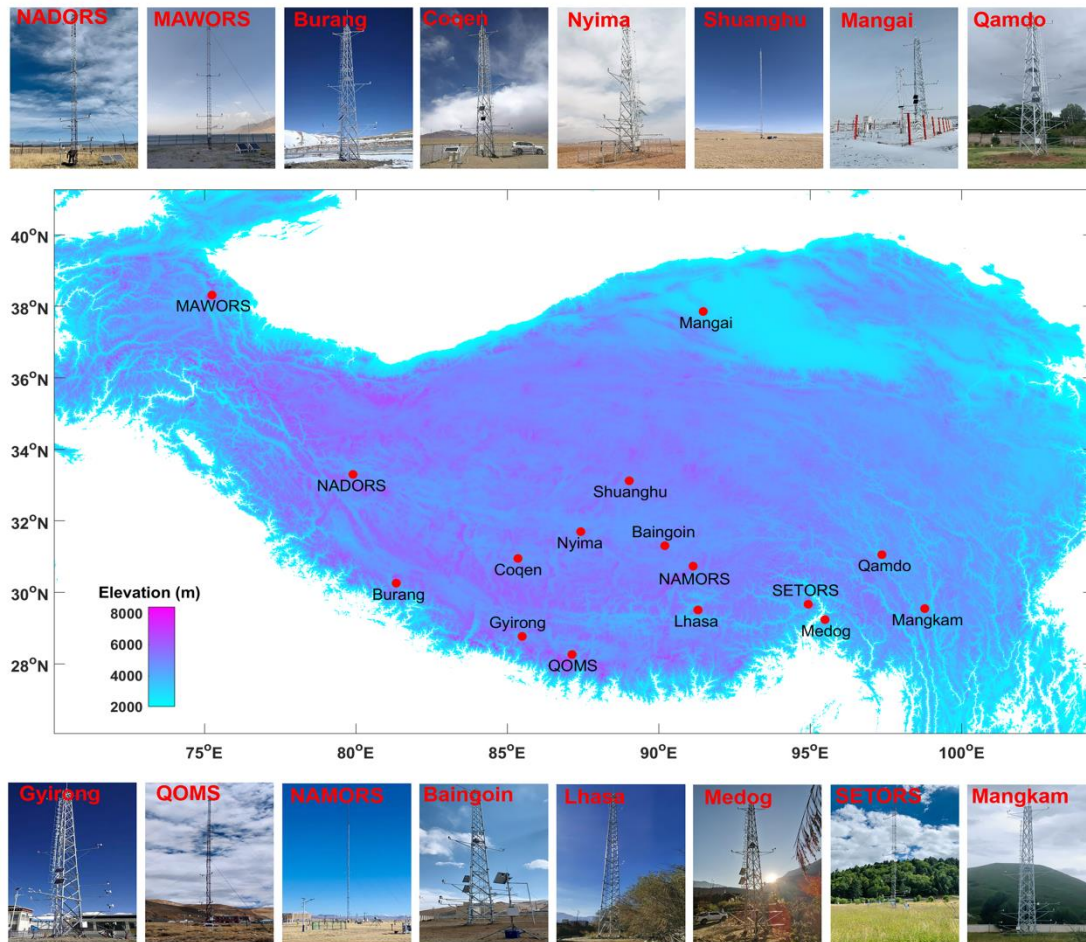
## 169 **2 The observation platform and methods**

### 170 **2.1 Introduction of observation platform and instruments configuration**

171 Long-term and quasi-continuous EC networks have been established worldwide across diverse  
172 ecosystems, including AmeriFlux and Fluxnet-Canada in North America, EuroFlux and CarboEurope in  
173 Europe, AsiaFlux and ChinaFlux in Asia, and OzFlux in Australia (Baldocchi, 2014; Yu et al., 2024).  
174 These networks provide critical ground-based measurements for understanding LA energy and material  
175 exchanges. Given the TP’s vast area (approximately 2.6 million km<sup>2</sup>) and extreme environmental  
176 conditions — such as high solar radiation, large diurnal temperature variations, and limited  
177 precipitation—such EC observations are especially valuable. In this context, the Institute of Tibetan  
178 Plateau Research, Chinese Academy of Sciences, established six comprehensive and long-term LA  
179 interaction stations in remote and data-scarce regions of TP gradually since 2004 (Ma et al., 2008),  
180 including QOMOS (the Qomolangma Atmospheric and Environmental Observation and Research  
181 Station, CAS), NAMORS (the Nam Co Monitoring and Research Station for Multisphere Interactions,  
182 CAS), SETORS (the Southeast Tibet Observation and Research Station for the Alpine Environment,  
183 CAS), NADORS (the Ngari Desert Observation and Research Station, CAS), MAWORS (the Muztagh  
184 Ata Westerly Observation and Research Station, CAS), and Shuanghu. Since 2019, the 6 stations were  
185 upgraded with new sonic anemometer and gas analyzer sensors gradually (CSAT3 and LI7500DS),  
186 enhancing the measurement capabilities. The instrumentation and long-term data at 5 stations covering  
187 2006–2021 can be found in Ma et al. [2020] and Ma et al. [2024].

188 Furthermore, the Second Tibetan Plateau Expedition and Research Program (STEP) in 2019 has  
189 expanded the network, adding 10 additional LA interaction stations, including Medog, Qamdo, Mangkam,  
190 Mangai, Baingoin, Nyima, Jyirong, Burang, Coqen, Lhasa, especially in the remote western and northern  
191 regions. The integrated EC devices (IRGASON, Campbell; CSAT3 & LI7500RS in Lhasa), capable of  
192 measuring high-frequency (10 Hz) quantities of sonic temperature, water, CO<sub>2</sub>, and three-dimensional  
193 winds, have been used. This expansion resulted in the creation of the Third Pole Environment Integrated  
194 Three-dimensional Observation and Research Platform (TPEITORP, observation platform for short  
195 hereafter) for measuring water, heat, and CO<sub>2</sub> fluxes over the TP (Ma et al., 2023). All stations are  
196 equipped with 20 m planetary boundary layer (PBL) towers (40 m at Lhasa) that continuously measure  
197 a comprehensive set of meteorological and flux variables. These include air pressure, liquid precipitation,  
198 infrared land surface temperature, four-component radiation, soil temperature and moisture at multiple  
199 depths, air temperature and humidity at five vertical levels, wind speed and direction at five levels, as  
200 well as turbulent fluxes of water, heat, and CO<sub>2</sub>. Turbulent fluxes were measured using an EC system  
201 installed on each tower, with sensor height and orientation optimized according to prevailing wind  
202 directions and local surface roughness conditions. The details of the instrument configuration, station  
203 locations, and photographs are provided in Table 1 and Fig. 1, respectively. In-situ measurements from  
204 these stations, with updated systems, were utilized to analyze the seasonal and diurnal variations of water,

205 heat, and CO<sub>2</sub> fluxes, as well as the associated energy budget and carbon source–sink dynamics across  
 206 contrasting ecosystems and climates. A detailed illustration of the observational environments at 16  
 207 stations are as follows.



208  
 209 **Figure 1.** The locations and photos of 16 LA interaction stations composing the comprehensive  
 210 observation and research platform over the TP. (All the photos have been taken by the authors)

211 QOMOS station is located in Rongbuk Valley, north of Mt. Everest, with a flat observation field  
 212 dominated by barren land and sparse vegetation. NAMORS station, on the southeast bank of the third  
 213 largest lake (Nam Co) in TP, is covered by alpine meadow. Both QOMOS and NAMORS have in situ  
 214 EC and PBL tower systems that have been in operation since 2005, with sensors upgraded in 2019.  
 215 SETORS station, located in a mountain valley in the southeast TP, is covered with dense vegetation (50–  
 216 60 cm high). The EC and PBL systems were first installed in 2007 and fully upgraded in 2020. NADORS  
 217 station, in grassland near Ritu County and Bangong Co, has had an EC system and an automatic weather  
 218 station (AWS) since 2008, with a new 20 m PBL tower and a new EC system installed in 2020. MAWORS  
 219 station, located near Mustag Mountain and Karakori Lake in Xinjiang, is influenced by westerly winds.  
 220 The station has been equipped with an EC system since 2010, and both EC and PBL systems were  
 221 updated in October 2020. Shuanghu station, located 3 km north of Shuanghu County, has been  
 222 operational since 2012, with a typical alpine grassland surface. The original EC system is still in use,  
 223 with new EC and PBL systems added in 2021.

224 Table 1. Overview of instruments configuration and settings at 16 stations, including observation

225 variables, instrument sensors, observational heights, latitude (lat), longitude (lon), altitude (alt) and  
 226 landscape at each station.

Variables	Sensors (Manufacturers)	Heights	Stations (lat, lon, alt, landscape)
Air temperature and humidity	HMP155A-L (Vaisala)	1.5, 2, 4, 10, and 20 m	1. QOMOS (28.36°N, 86.95°E, 4276 m, Alpine desert);
Wind speed and direction	05103-L (R.M.Young)	1.5, 2, 4, 10, and 20 m	2. NAMORS (30.77°N, 90.98°E, 4730 m, Alpine steppe);
Air pressure	CS106 (Vaisala)	-	3. SETORS (29.77°N, 94.73°E, 3327 m, Alpine meadow);
Radiations	CNR4 (Kipp & Zonen)	1.5 m	4. NADORS (33.39°N, 79.7°E, 4270 m, Alpine desert);
Precipitation	RG3 (Onset)	-	5. MAWORS (38.41°N, 75.05°E, 3668 m, Alpine desert);
Soil temperature and moisture	CS655 (Campbell)	0.1, 0.2, 0.4, 0.8 and 1.6 m	6. Shuanghu (33.22°N, 88.83°E, 4947 m, Alpine steppe);
Soil heat flux	HFP01 (Hukseflux)	0.1 and 0.2 m	7. Lhasa (40.01 °N, 116.38 °E, 3650 m, City)
Turbulent flux	CSAT3B (Campbell); LI-7500DS (Li-COR)	Site specific	
Air temperature and humidity	HMP155A (Vaisala)	1, 2, 4, 10 and 20 m	8. Medog (29.32°N, 95.29°E, 820 m, Forest);
Wind speed and direction	05103 (R.M.Young)	1, 2, 4, 10 and 20 m	9. Qamdo (31.15°N, 97.17°E, 3307 m, Alpine steppe);
Air pressure	PTB110 (Vaisala)	-	10. Mangkam (29.64°N, 98.59°E, 3840 m, Alpine meadow);
Radiations	CNR4 (Kipp & Zonen)	1.5 m	11. Mangai (37.95°N, 91.7°E, 3073 m, Bare ground);
Precipitation	RG3 (Onset)	-	12. Baingoin (31.4°N, 90.01°E, 4709 m, Bare ground);
Soil temperature and moisture	CS655 (Campbell)	0.1, 0.2, 0.4, 0.8, 1.6 m	13. Nyima (31.79°N, 87.23 °E, 4573 m, Alpine steppe);
Soil heat flux	HFP01 (Hukseflux)	0.1 and 0.4 m	14. Jyirong (28.86 °N, 85.29 °E, 4140 m, Bare ground);
Turbulent flux	IRGASON (Campbell)	Site specific	15. Burang (30.35 °N, 81.14 °E, 4113 m, Bare ground);
			16. Coqen (31.04 °N, 85.16 °E, 4683 m, Alpine steppe);
Notes: the heights of turbulent flux measurements from station number 1 to number 16 are 3.0 m, 3.77 m, 3.13 m, 3.7 m, 3 m, 3.2 m, 5 m, 5.5 m, 5.5 m, 3.5 m, 3.5 m, 5.5 m, 3.8 m, 3.5 m, 3.5 m and 40 m respectively. In Lhasa station, the heights of atmosphere variables at 5 layers are 2 m, 4 m, 8 m, 16 m, 32 m.			

227 The stations of Medog, Qamdo, Mangkam, Mangai, Baingoin, Nyima, Jyirong, Burang, Coqen and  
 228 Lhasa were gradually established till 2021 with support from STEP program. Medog, Qamdo, and  
 229 Mangkam stations are located in the southeastern TP. Medog is located at the southern foot of the eastern  
 230 Himalayas, near the Yarlung Zangbo River, with a steep terrain surrounded by subtropical evergreen  
 231 broadleaf forest (i.e. banana trees) and crops (i.e., peanuts). Qamdo is situated in the Changdu  
 232 Meteorological Bureau's observation field, covered by grass at the top of hilly Changdu City. Mangkam  
 233 is located at the Mangkang County Meteorological Bureau's external observation field, with a surface

234 covered by 10 cm grass. Mangai station is in the northern part of the TP, with a Gobi desert landscape.  
235 The PBL tower and EC system were mounted on the Mangai Meteorological Bureau's external  
236 observation field. Baingoin, Nyima, and Coqen stations are located in the west-central TP, each with PBL  
237 and EC systems installed at their respective County Meteorological Bureau's observation fields. The land  
238 surfaces are bare ground, alpine meadow and alpine meadow, respectively. Jyirong and Burang, located  
239 north of the Himalayas, are covered by sparse vegetation and bare land, respectively. Lhasa station,  
240 constructed in 2020 and having a 40 m PBL tower, is located in the field observation base of ITPCAS,  
241 with roads and low-level buildings surrounded.

242 These stations are distributed across various climatic and environmental regions, covering  
243 landscapes such as alpine desert, alpine steppe, alpine meadow, bare ground and city. Some stations,  
244 including Mangkam, Baingoin, Qamdo and Lhasa are situated in or adjacent to cities, thus they can be  
245 influenced by nearby human activities to some extent. The land surface properties (e.g., land cover,  
246 terrain, soil texture) and local climate vary markedly across stations, providing valuable data for  
247 generalizing LA interaction schemes across diverse environments and climates over the TP. These  
248 differences highlight the complexity of coupled LA interactions, the challenges in obtaining necessary  
249 data for model development, and the need for a comprehensive understanding of how land surface  
250 processes affect atmospheric conditions and climate predictability. After the construction of the  
251 observation platform in 2021, the instruments calibration and maintenance have been carried out twice a  
252 year, with field work distance of more than 5000 km and duration of more than 1 month each time. Our  
253 efforts to maintain this observation platform aim to bridge the observational gaps in data-scarce regions  
254 and to support research on land surface processes, water and energy cycles, and environmental effects  
255 across the TP.

## 256 **2.2 Methods for data processing and analyzing**

257 To study the spatial-temporal variations of meteorological variables and turbulent fluxes of water,  
258 heat and CO<sub>2</sub> at these stations and to analyze the influencing factors over the different climatic and  
259 environmental conditions, 15 stations have been chosen in this study with an exception of Lhasa, which  
260 only captured the measurements during the daytime because of the power malfunction at night. We  
261 selected field measurements of more than 2 years, mostly covering the period of May 2021 to July 2023.  
262 The proportions of data coverage for meteorological variables and turbulent flux are close to 94% and  
263 77%, respectively, with the least data integrity percentage of approximately 50% in Mangai station.  
264 Details of data coverage at each station can be found in Table S1 in supplementary material. After  
265 accounting for data losses due to instrument failure, power interruptions, and occasional human  
266 operational errors, precipitation records from July 2021 to June 2022 were used in this study.  
267 Precipitation data gaps occurred at three stations—QOMS (20 %, Feb 1 – Feb 14, May 14 – Jun 1, 2022),  
268 NAMORS (22 %, Jan 1 – Mar 21, 2022), and SETORS (6 %, Feb 8 – Feb 12, Mar 27 – Apr 12, 2022)—  
269 with the missing periods distributed intermittently throughout the observation year. These data gaps were  
270 primarily caused by technical or operational issues. As the rain gauge (RG3, Onset) measures only liquid  
271 precipitation during warm seasons and does not record solid precipitation in cold months, the missing  
272 data, mostly during winter and pre-monsoon periods, do not affect the conclusions regarding the spatial  
273 and temporal variations of liquid precipitation.

274 Currently, meteorological variables were processed following standardized protocols. Abnormal  
 275 values—defined as physically implausible measurements such as downward shortwave radiation greater  
 276 than  $1360 \text{ W m}^{-2}$  or less than  $0 \text{ W m}^{-2}$ , or variables showing unrealistic diurnal or seasonal patterns caused  
 277 by sensor or power malfunctions—were flagged and removed after visual inspection and consistency  
 278 checks. For turbulent heat flux, two types of open-path EC systems were used across the stations:  
 279 CSAT3B and LI-7500DS (stations 1–7) and IRGASON (stations 8–16). These high frequency data were  
 280 processed using standard EddyPro software, which includes standard procedures of spike removal,  
 281 buoyancy flux conversion to sensible heat, double rotation, as well as ultrasonic virtual temperature  
 282 correction and density correction (Webb-Pearman-Leuning correction) (Massman and Lee, 2002;  
 283 Mauder and Foken, 2006; Twine et al., 2000). Quality flags are applied to the flux estimates, considering  
 284 steady state test and integral turbulence characteristics test (Mauder et al., 2013). *NEE* represents the net  
 285 vertical  $\text{CO}_2$  flux between the ecosystem and the atmosphere and is directly measured by the EC system.  
 286 The two main components of the carbon cycle, *GPP* and *Re*, are then estimated from the measured *NEE*  
 287 using the standard flux partitioning procedures implemented in the REddyProc package (Wutzler et al.,  
 288 2018), where a temperature response function for *NEE* fluxes is used to represent *Re*, with *GPP* derived  
 289 as the difference between *Re* and *NEE*. Nighttime *NEE* data with low friction velocity were filtered to  
 290 avoid biases, and gaps were filled using the available meteorological data. Specifically, the friction  
 291 velocity threshold was estimated using the bootstrapping approach implemented in REddyProc,  
 292 following the standard procedure described by Wutzler et al. (2018). Flux gap-filling was performed  
 293 using the marginal distribution sampling method within REddyProc, which estimates missing values  
 294 based on relationships with radiation, air temperature, and vapor pressure deficit within a 7-14 day  
 295 moving window. Quality control procedures included removing data points affected by sensor  
 296 malfunction, spikes, or physically implausible fluxes, and applying the flagging schemes of Mauder et  
 297 al. (2013). All low-quality or filtered data were excluded prior to gap-filling and flux partitioning to  
 298 ensure data integrity.

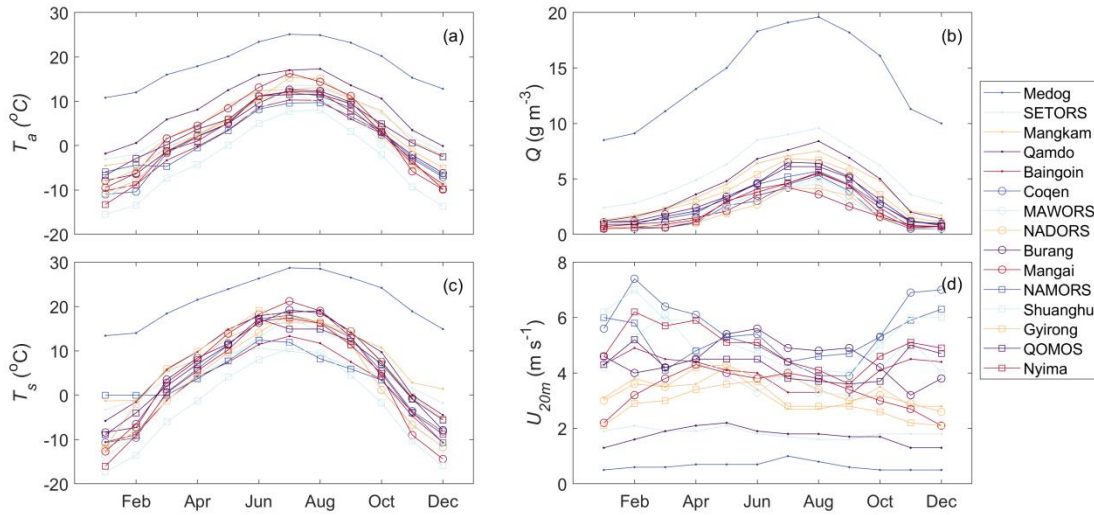
299 Diurnal and seasonal variations of meteorological and turbulent flux variables were analyzed after  
 300 filtering out low-quality and spurious data. To reduce the influence of data gaps and enhance  
 301 comparability among sites, monthly averaged diurnal cycles of meteorological variables and turbulent  
 302 fluxes were used to examine their spatial and temporal patterns across stations. The total annual values  
 303 for *ET*, *NEE*, *GPP* and *Re* were obtained by summing the monthly values. During data quality screening,  
 304 three stations (QOMOS, NAMORS, and Baingoin) were excluded from the *NEE* flux synthesis because  
 305 their *NEE* diurnal cycles exhibited physically inconsistent behavior. Specifically, QOMOS and  
 306 NAMORS showed inverted daytime-nighttime variations, while Baingoin displayed abnormally  
 307 nighttime  $\text{CO}_2$  emissions, probably influenced by nearby biomass burning. Only the remaining 12  
 308 stations with reliable  $\text{CO}_2$  flux data were retained for spatial and temporal analyses. The energy budget  
 309 ratio (*EBR*) and Bowen ratio (*Bo*) at each station were estimated to evaluate energy conditions and energy  
 310 consumption. *EBR* ( $EBR = \frac{\sum LE + SH}{\sum R_n - G}$ ) compares the cumulative sum of available energy inputs to the  
 311 cumulative sum of turbulent energy outputs over an entire year. Available energy inputs include net  
 312 radiation ( $R_n$ ,  $\text{W m}^{-2}$ ) and ground heat flux ( $G$ ,  $\text{W m}^{-2}$ ) while turbulent energy outputs include latent heat  
 313 flux ( $LE$ ,  $\text{W m}^{-2}$ ) and sensible heat flux ( $SH$ ,  $\text{W m}^{-2}$ ). Net radiation can be measured by four components  
 314 radiation sensors and is expressed as the difference between downward and upward shortwave ( $R_{s\downarrow}$  and  
 315  $R_{s\uparrow}$ ,  $\text{W m}^{-2}$ ) and longwave radiation ( $R_{l\downarrow}$  and  $R_{l\uparrow}$ ), specifically:  $R_n = R_{s\downarrow} + R_{l\downarrow} - R_{s\uparrow} - R_{l\uparrow}$ . Bowen

316 ratio ( $Bo = \frac{SH}{LE}$ ) indicates the relative proportions of energy consumption between  $SH$  and  $LE$ . Typically,  
 317  $Bo$  is high under dry conditions and low under wet conditions.

### 318 3 Results and discussions

#### 319 3.1 The spatial-temporal variations of atmospheric meteorological variables

320



321

322 **Figure 2.** The seasonal variations of meteorological variables, including (a) air temperature ( $T_a$ ), (b)  
 323 air humidity ( $Q$ ); (c) land surface temperature ( $T_s$ ); (d) wind speed at 20 m height ( $U_{20m}$ ).

324

325 The 15 stations are distributed across diverse environments and climates, resulting in considerable  
 326 variations in the seasonal patterns of air temperature ( $T_a$ ), air humidity ( $Q$ ), wind speed ( $U_{20m}$ ) and land  
 327 surface temperature ( $T_s$ ) (Fig. 2 and Table 2). The details of seasonal variations of the monthly average  
 328 and annual mean of air temperature, wind speed and absolute humidity at the 15 stations can be found in  
 329 Table S2-S4. The annual average  $T_a$ ,  $T_s$ ,  $Q$  and  $U_{20m}$  span at ranges of  $-3.5\sim 18.5$  °C,  $-3.5\sim 21.6$  °C,  
 330  $1.88\sim 14.1$   $g\ m^{-3}$  and  $0.6\sim 5.6$   $m\ s^{-1}$ , respectively. The annual average  $T_a$  shows strong positive  
 331 correlations ( $r$ ) with annual average  $T_s$  ( $r = 0.99, p < 0.01$ ) and downward long-wave radiation ( $R_{L\downarrow}$ ,  $r =$   
 332  $0.84, p < 0.01$ ), and a notable negative correlation with downward short-wave radiation ( $R_{S\downarrow}$ ,  $r = -0.72,$   
 333  $p < 0.01$ ) (Fig. S1). The high correlation with  $T_s$  indicates that strong LA coupling governs the spatial  
 334 distribution of  $T_a$ , while the negative correlation with  $R_{S\downarrow}$  reflects the impact of cloud cover, which  
 335 reduces  $R_{S\downarrow}$  but increases  $T_a$ . Additionally, the annual average  $T_a$  exhibits a significant negative  
 336 correlation with elevation ( $r = -0.92, p < 0.01$ ). The highest annual average  $T_a$  ( $18.5^\circ\text{C}$ ) occurs at Medog  
 337 station (820 m a.s.l.), while the lowest ( $-3.5^\circ\text{C}$ ) is observed at Shuanghu station (4947 m a.s.l.). Stations  
 338 such as Qamdo (3307 m a.s.l.), SETORS (3327 m a.s.l.), Mangkam (3840 m a.s.l.), and Mangai (3073  
 339 m a.s.l.) have annual average values ranging from  $5.2^\circ\text{C}$  to  $8.6^\circ\text{C}$ , whereas stations above 4000 m have  
 340 annual averages from  $-3.5^\circ\text{C}$  to  $3.9^\circ\text{C}$ . Seasonal variations in  $T_a$  can also be influenced by climatic and  
 341 environmental conditions. For example, despite similar elevations (around 3300 m a.s.l.) and low wind  
 342 speeds (approximately  $1.8\ m\ s^{-1}$ ), Qamdo shows larger annual value and amplitude in  $T_a$  than that in  
 343 SETORS, and it may be attributed to the former's lower moisture condition as well as the strong "urban  
 344 heat island" effect. Qamdo, having lower annual precipitation value, is located at a mountaintop grass  
 land observation field in the city center, thus, relatively weak evaporated cooling and intense human

345 activities and infrastructure may contribute to Qamdo's elevated  $T_a$ . Similarly, in Baingoin and  
 346 NAMORS, despite their proximity and similar elevations, NAMORS experiences higher  $T_a$  from  
 347 October to February and lower temperatures from March to August. Such variations are likely influenced  
 348 by the large lake (Nam Co), which has a cooling effect in summer and a warming effect in winter.  
 349 Table 2. The annual average meteorological variables, soil water contents ( $SM_{10cm}$  and  $SM_{160cm}$   
 350 indicate soil moisture at 10 cm and 160 cm, respectively),  $NEE$ ,  $GPP$ ,  $Re$ ,  $ET$ ,  $EBR$  and  $Bo$  at 15 stations.

Sites	$T_a$ (°C)	$Q$ (g $m^{-3}$ )	$U_{20m}$ (m $s^{-1}$ )	$T_s$ (°C)	$Prec$ (mm)	$SM_{10cm}$ (%)	$SM_{160cm}$ (%)	$NEE$ (g C $m^{-2}a^{-1}$ )	$GPP$ (g C $m^{-2}a^{-1}$ )	$Re$ (g C $m^{-2}a^{-1}$ )	$ET$ (mm)	$EBR$ (-)	$Bo$ (-)
Medog	18.5	14.1	0.6	21.6	2164	9 - 25	18 - 43	365	885	1193	571	1.04	0.46
SETORS	5.7	5.64	1.8	6.1	1053	32 - 42	20 - 50	-153	754	633	381	0.634	0.84
Mangkam	5.2	4.07	3.3	6.2	596	4 - 16	20 - 41	-121	454	192	345	0.683	1.09
Qamdo	8.6	4.3	1.7	9.0	456	4 - 14	8 - 19	-133	486	443	354	0.650	0.73
Baingoin	0.5	2.38	4.1	1.2	392	3 - 22	1 - 12	Nan	Nan	Nan	208	0.680	1.52
NAMORS	1.3	2.80	5.2	2.6	304	1 - 9	3 - 6	Nan	Nan	Nan	348	0.828	1.64
Shuanghu	-3.5	2.10	5.3	-3.5	246	1 - 10	9 - 38	-86	165	75	174	0.836	1.88
Gyirong	2.9	3.53	2.8	4.3	237	5 - 14	8 - 20	-58	249	189	218	0.641	2.35
QOMOS	3.9	2.98	4.3	5.6	196	2 - 9	2 - 3	Nan	Nan	Nan	115	0.797	4.11
Nyima	1.3	2.28	4.9	2.3	182	3 - 14	0 - 2	-13	56	36	194	0.631	2.02
Coqen	1.6	2.03	5.6	1.8	137	2 - 6	4 - 9	-15	146	260	155	0.821	3.94
MAWORS	0.8	2.23	4.3	1.0	107	1 - 9	1 - 29	-157	538	368	344	0.623	1.31
NADORS	2.4	1.88	3.5	3.0	64	12 - 48	20 - 50	-174	415	238	222	0.646	0.99
Burang	2.5	3.12	4.5	3.1	58	1 - 4	1 - 5	-65	100	33	121	0.659	4.10
Mangai	3.5	1.93	3.4	4.8	43	1 - 2	1 - 2	-3	69	20	76	0.747	8.32

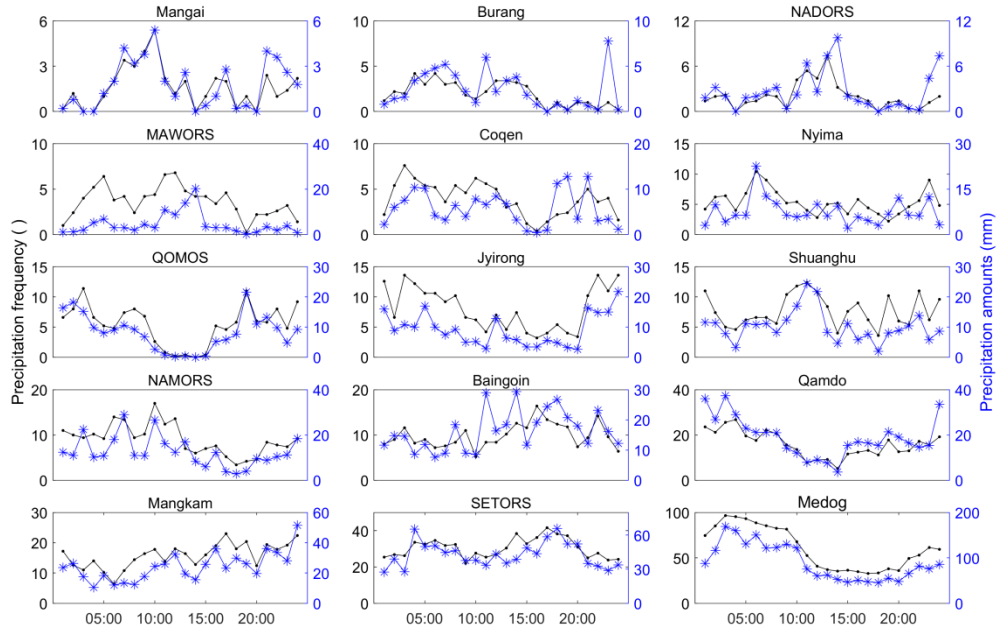
351 Both air humidity ( $Q$ ) and wind speed at a 20 m height ( $U_{20m}$ ) at 15 stations show similar  
 352 seasonal variations (Fig. 2b and 2d). Generally, the seasonal patterns of  $Q$  and  $U_{20m}$  are influenced  
 353 by the interaction of monsoon and westerly systems. Seasonally, the summer monsoon system leads  
 354 to the lower values in  $U_{20m}$  and higher values in  $Q$ , while high values in  $U_{20m}$  and low values in  $Q$   
 355 during winter are coincident with the dominating westerly system. Spatially,  $Q$  decreases from  
 356 southeast to northwest across the TP. Medog station, located in a subtropical forest climate, exhibits  
 357 the highest annual average  $Q$  of 14.1 g  $m^{-3}$ . The higher group of annual average  $Q$  values are found  
 358 at SETORS (5.61 g  $m^{-3}$ ), Qamdo (4.28 g  $m^{-3}$ ), and Mangkam (4.12 g  $m^{-3}$ ), while the rest of the  
 359 stations range from 1.74 to 3.67 g  $m^{-3}$ . Further, both the annual averages of  $Q$  and  $U_{20m}$  correlate  
 360 with elevation, showing negative and positive correlations of -0.88 ( $p < 0.01$ ) and 0.83 ( $p < 0.01$ ),  
 361 respectively (Fig. S1).  $U_{20m}$  is the lowest in Medog, Qamdo, and SETORS, where wind speeds are  
 362 generally under 2  $m s^{-1}$ , primarily because of their locations in the southeast mountainous regions.  
 363 Conversely, stations at higher elevations with more homogeneous landscapes, such as Nyima,  
 364 Coqen, and Shuanghu, experience the highest wind speed.

365 Overall, the 15 stations reveal distinct spatial and seasonal variability in meteorological  
 366 conditions across the TP, driven primarily by elevation and large-scale circulation systems. The  
 367 combined effects of topography, monsoon and westerly influences, and local factors such as  
 368 urbanization and lake regulation shape the observed gradients in temperature, humidity, and wind  
 369 speed.

### 370 **3.2 The spatial-temporal variations of liquid precipitation and soil water content**

371 The wet-dry condition at each station is mostly correlated with liquid precipitation and soil  
372 water content (Table 2). The highest annual precipitation occurs in the southeastern TP, at stations  
373 like Medog, SETORS, Mangkam, and Qamdo, where the monsoon system dominates. The monsoon  
374 system can bring moist air into the plateau, resulting in annual precipitation values of 2164 mm in  
375 Medog, 1053 mm in SETORS, 596 mm in Mangkam, and 456 mm in Qamdo. In contrast, stations  
376 with low annual precipitation, such as Mangai, Burang, NADORS, and MAWORS, are located in  
377 the western and northern parts of the TP, where mid-latitude westerlies prevail, with annual  
378 precipitation below 120 mm. The rest seven stations in the central and western TP, where both  
379 westerly and monsoon systems interact, experience annual precipitation ranging from 120 mm to  
380 400 mm. Specifically, Baingoin, NAMORS, and Shuanghu, located in the central TP, receive annual  
381 precipitation of between 200 mm and 400 mm, while Nyima, Coqen, Gyirong, and QOMOS  
382 receive 100 mm to 200 mm per year. This pattern of high in the southeast and low in the northwest  
383 aligns with the Global Precipitation Measurement (GPM) product (Li et al., 2021a). The spatial  
384 distribution of soil water content at depths of 10 cm and 160 cm generally mirrors the precipitation  
385 pattern, but they can be also influenced by soil properties and local conditions. For example,  
386 NADORS, situated near Bangong Co, exhibits the highest soil water content at 10 cm depth. At 160  
387 cm depth, stations like Shuanghu, NADORS, MAWORS, and Gyirong show soil water content up  
388 to 0.20, indicating pronounced groundwater contribution. In contrast, Mangai, Burang, Coqen, and  
389 NAMORS have the lowest soil water contents.

390 Seasonally, liquid precipitation over the TP is primarily concentrated during the summer  
391 monsoon seasons, with peaks in July and August (Fig. S3), consistent with findings from Yang et  
392 al. (2023) in central TP. Chen et al. (2023) observed that monthly precipitation in the Yarlung  
393 Tsangbo Grand Canyon exhibits two peaks, one in April and the other in August, which is also the  
394 case for SETORS and Medog. Diurnally, Li et al. (2021b) noted that summer precipitation over the  
395 TP often occurs in the afternoon and evening. However, the diurnal patterns vary markedly across  
396 the 15 stations (Fig. 3). Precipitation frequency and amounts followed similar diurnal variations,  
397 with notable exceptions at Baingoin and MAWORS, where precipitation frequency peaked between  
398 6:00 and 11:00, but the highest rainfall amounts occurred at 14:00. At westerly-dominated stations  
399 in the northern TP like Mangai, NADORS, MAWORS, and Shuanghu, precipitation peaks during  
400 the day and is minimal at night, though the timing of these peaks varies. In contrast, stations in  
401 mountainous regions—Medog, Mangkam, Qamdo, Nyima, and Gyirong—experience peak  
402 precipitation mostly at night, similar to findings in Chen et al. (2023) for the Yarlung Zangbo Grand  
403 Canyon. SETORS, QOMOS, and Coqen exhibit bimodal precipitation patterns, with peaks at night  
404 and in the late afternoon. Burang and NAMORS show higher precipitation in the first half of the  
405 day, with lower amounts later, and such patterns are probably related with the lake breeze circulation.  
406 Generally, daytime rainfall is probably driven by up-slope flows due to surface heating, while the  
407 monsoon nocturnal low-level jet may contribute to nighttime rainfall. Further, the local circulations  
408 of lake-land breeze and mountain-valley breeze can also modulate the water circulations and impact  
409 on the diurnal variation of precipitation.



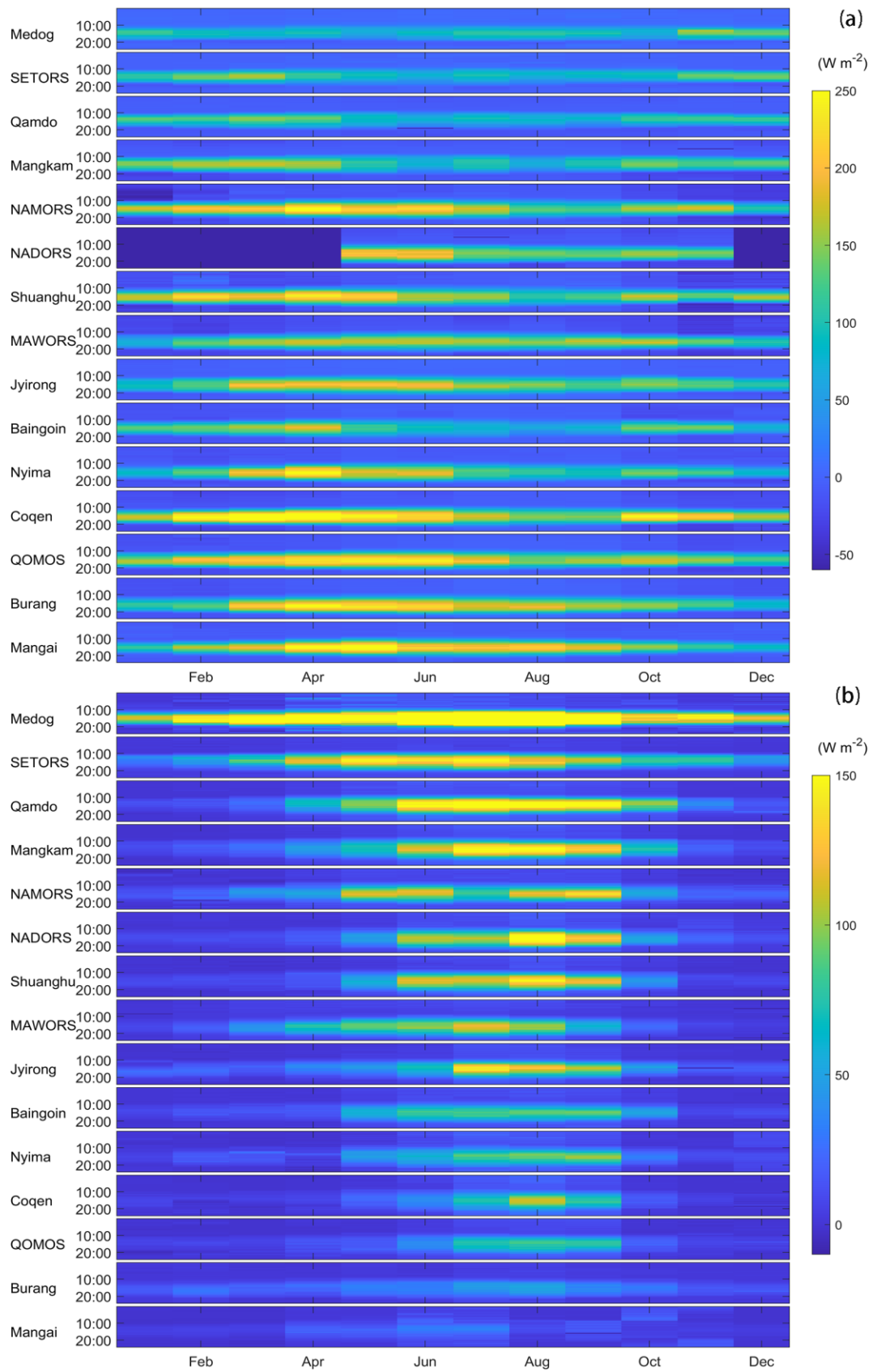
410

411 **Figure 3.** The diurnal variations of liquid precipitation amounts and frequency at 15 stations. Liquid  
 412 precipitation frequency indicates the total times of liquid precipitation annually.

413 Overall, precipitation and soil moisture across the TP show a clear southeast–northwest  
 414 gradient, decreasing from humid monsoon regions to arid westerly-dominated areas. Seasonal and  
 415 diurnal variations reflect the combined influence of the summer monsoon, local topography, and  
 416 mesoscale circulations such as mountain–valley and lake–land breezes. These spatial and temporal  
 417 patterns highlight strong hydroclimatic heterogeneity and its control on regional LA coupling.

418 **3.3 The spatial-temporal variations of energy flux**

419 Net radiation ( $R_n$ ) provides the energy source for LA energy and material exchange, and is  
 420 mainly divided into three components: ground heat flux ( $G$ ),  $SH$ , and  $LE$ .  $R_n$  generally shows  
 421 positive values in its seasonal variations, indicating that the ground surface acts as a heat source  
 422 relative to the overlying atmosphere.  $R_n$  peaks in June or July and reaches its lowest in December  
 423 or January. SETORS and Gyirong have monthly  $R_n$  values of greater than  $90 \text{ W m}^2$ , while Baingoin  
 424 and Mangai have values of below  $70 \text{ W m}^2$ . The other stations show values of between  $70$  and  $90 \text{ W}$   
 425  $\text{m}^2$ , which are similar to those reported in previous studies, 4 stations over the TP and 4 stations in  
 426 the lower reaches of the Yangtze River region (Yao et al., 2024). Details for the seasonal variation  
 427 of monthly net radiation and monthly ground heat flux and their annual means at the 15 stations can  
 428 be found in Table S5-S6. Further, heat storage occurs mainly from March to August, peaking around  
 429 June, while heat release is most remarkable from October to February, with the largest release in  
 430 December. The annual average of monthly  $G$  ranges from  $-0.01 \text{ W m}^2$  at Qamdo to  $2.39 \text{ W m}^2$  at  
 431 NADORS. The close-to-zero  $G$  values suggest minimal impact of ground heat storage on the energy  
 432 budget at an annual scale, while the dominating positive values suggest a warming trend in the  
 433 ground, aligning with global warming and the rise in land surface temperature (Duan and Xiao,  
 434 2015; Oku et al., 2006; Zhang et al., 2023).



435

436

437

**Figure 4.** The heat maps for averaged diurnal and seasonal variations of sensible heat flux (a) and latent heat flux (b) at 15 stations.

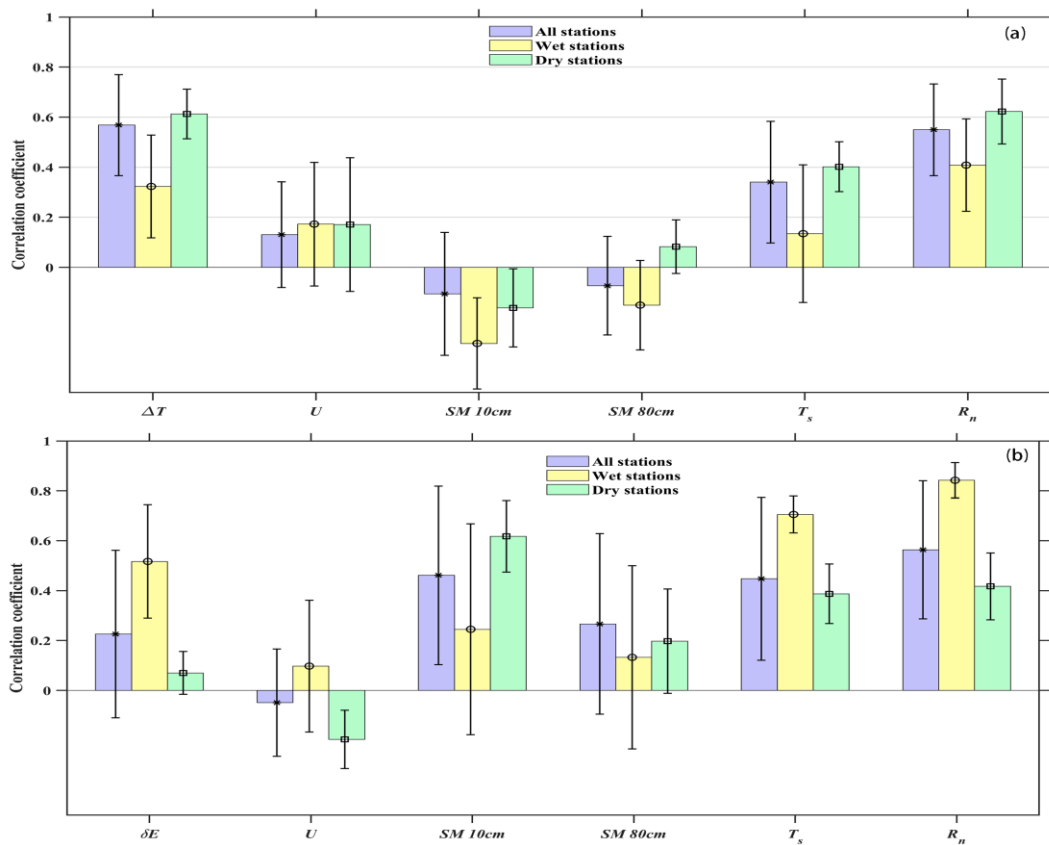
438 Turbulent heat fluxes, including  $SH$  and  $LE$ , exhibit clear diurnal and seasonal variations (Fig.  
439 4), consistent with previous studies on the TP (Ma et al., 2005; Zhong et al., 2019a). In addition, the  
440 seasonal evolution of monthly averaged diurnal  $SH$  and  $LE$  can be found in Fig. S4-S5.  $SH$  peaks  
441 during the pre-monsoon months of April and May, and is lowest in the cold months of December  
442 and January. Stations with sufficient water availability, such as Medog, SETORS, Mangkam,  
443 Qamdo, Baingoin, MAWORS, and NADORS, have total annual  $SH$  values ranging from 269 to 356  
444  $W m^{-2}$ . The first five stations receive high precipitation, while the latter two have substantial soil  
445 moisture supply. Other stations have total annual  $SH$  fluxes exceeding  $400 W m^{-2}$ , with QOMOS  
446 and Coqen reporting the highest annual values of  $582 W m^{-2}$  and  $626 W m^{-2}$ , respectively.  $LE$  peaks  
447 during the monsoon seasons (July to August) and is not apparent throughout the cold months.  
448 Specifically, the total annual  $LE$  is only  $61.3 W m^{-2}$  at the extremely dry Mangai station, while  
449 Medog records monthly  $LE$  values all exceeding  $29 W m^{-2}$ . Spatially,  $LE$  is showing decreasing  
450 pattern from the southeast wet regions to the northwest dry regions. As shown in Table 1, the  $Bo$   
451 reflects the energy distribution between  $SH$  and  $LE$ . Medog, SETORS, and Qamdo in the southeast  
452 have  $Bo$  values of less than 1, indicating dominant heat consumption through the  $LE$ , while Mangai,  
453 Burang, and QOMOS in the northern and western regions have  $Bo$  ratios greater than 4, suggesting  
454 the dominant role of  $SH$ .

455 The  $EBR$  is the ratio of turbulent energy fluxes ( $SH + LE$ ) to available energy ( $R_n - G$ ). The  
456 average  $EBR$  across the 15 stations is approximately 0.73, ranging from 0.62 to 1.04, with 11 stations  
457 between 0.6 and 0.8, while Medog exceeds 1 (Table 2). These values are consistent with results  
458 from global eddy flux sites (Wilson et al., 2002). Imperfect energy balance closure can arise from  
459 several factors (Foken, 2008; Mauder et al., 2020), including footprint mismatch, instrumental  
460 biases, unaccounted energy storage, flux losses at different frequencies, and neglected advection.  
461 The influence of these factors likely varies among sites according to their surface heterogeneity and  
462 terrain complexity. A detailed site-level attribution of  $EBR$  differences requires further analysis and  
463 will be addressed in future work.

464 Following the LA interaction theories,  $SH$  ( $LE$ ) are primarily influenced by land-atmosphere  
465 temperature gradients ( $\Delta T = T_s - T_a$ ) or water vapor deficit ( $\Delta E = e_s - e_a$ , where  $e_s$  and  $e_a$  are the  
466 saturation vapor pressure and the actual vapor pressure respectively), wind speed ( $U$ ), soil moisture  
467 at 10 cm and 80 cm, land surface temperature ( $T_s$ ) and net radiation ( $R_n$ ), etc (Wang et al., 2017).  
468 The correlation coefficients between  $SH$  ( $LE$ ) and the related variables can be found in Table S7,  
469 and the dominating factors for LA turbulent flux are pronouncedly different under dry and wet  
470 stations, where energy-related variables are most important in water-sufficient conditions, while  
471 water-related variables show dominant role in water-shortage conditions. For example, wet stations  
472 such as Medog, SETORS, Mangkam, and Qamdo, which receive substantial precipitation and  
473 maintain high soil moisture, exhibit stronger correlations of  $LE$  with  $R_n$  and  $T_s$  than with soil  
474 moisture. In contrast, dry stations such as QOMOS, Nyima, Coqen, and Burang, characterized by  
475 low precipitation and limited soil moisture, show higher correlations of  $LE$  with soil moisture at 10  
476 cm than with other variables. Mangai, an extremely dry station with annual precipitation value of  
477 only 43.2 mm and very low soil moisture conditions (0.01-0.02), has the smallest annual  $ET$  value  
478 and no obvious correlations with all the variables. In NADORS, the annual  $ET$  has a value of 222.4  
479 mm, significantly higher than the annual precipitation amount of 64 mm, and the volumetric water

480 content at 80 cm can reach up to 0.3, suggesting a substantial impact of groundwater supply. Thus,  
 481 soil moisture and  $R_n$  have comparable high correlation coefficients in NADORS.

482 The correlation coefficients between  $SH$  ( $LE$ ) and related environment variables under  
 483 conditions of all stations, wet stations (Medog, SETORS, Mangkam, and Qamdo) and dry stations  
 484 (QOMOS, Nyima, Coqen, Burang) are grouped in Fig. 5. For all stations included,  $SH$  variations  
 485 are primarily driven by  $\Delta T$ , followed by  $R_n$  and  $T_s$ , with correlation coefficients of 0.57, 0.55 and  
 486 0.34, respectively (Fig. 5a). Further,  $SH$  has a positive correlation with wind speed and a negative  
 487 correlation with soil moisture. The correlation coefficients show large diversity under dry and wet  
 488 conditions, with generally lower values in wet stations than those in dry stations. For example, the  
 489 averaged correlation coefficients between  $SH$  and  $\Delta T/R_n/T_s$  under dry stations are 0.63/0.65/0.44  
 490 while those values (0.32/0.40/0.13) are much smaller under wet conditions. Wind speed has weaker  
 491 correlation with  $SH$ . but in MAWORS and Medog, the correlation coefficients could approach to  
 492 0.5. In NAMORS, there is a negative correlation between wind speed and  $SH$ . These phenomenons  
 493 may be related with the local circulations of mountain-valley and lake-land breezes, which may lead  
 494 to synchronized and opposite variations in such conditions.



495

496 **Figure 5.** The correlation coefficients between sensible heat flux (a), latent heat flux (b) and related  
 497 environmental variables at a temporal resolution of hourly under conditions of all stations, wet stations  
 498 and dry stations, respectively. The statistical significance of the correlation coefficients for each station  
 499 is provided in Table S7.

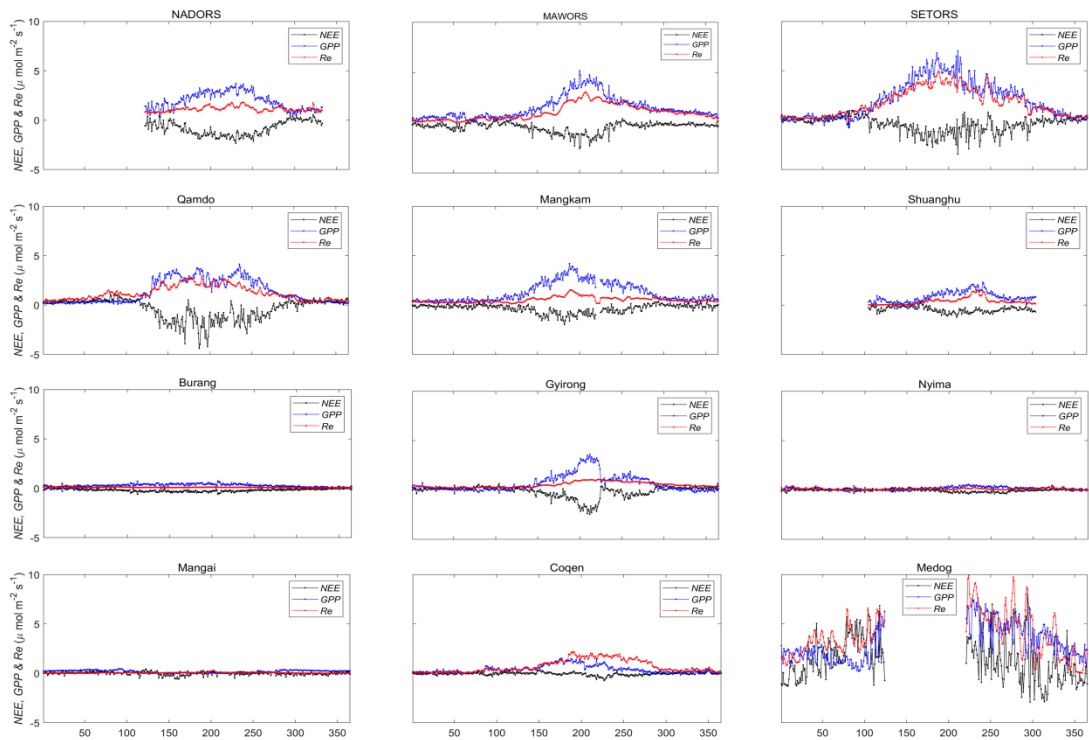
500 The correlations between  $LE$  and environmental variables are more complex (Table S7 and Fig.  
501 5b). The three paramount factors are  $R_n$ ,  $T_s$  and soil moisture at 10 cm, with correlation  
502 coefficients of 0.56, 0.46, 0.45, respectively. For wet stations, the most important variables are  
503 energy related variables ( $R_n$  and  $T_s$ ). Stations such as Medog, Mangkam, SETORS, Qamdo,  
504 Gyirong, and NADORS follow this pattern, with the first four stations influenced by high  
505 precipitation and the latter two by soil water content.  $\Delta E$  represents the difference between the  
506 actual and saturation vapor pressure, indicating the atmospheric moisture deficit. The saturation  
507 vapor pressure increases exponentially with temperature—by about 6 – 7% per degree Celsius—so  
508 warmer air can hold substantially more water vapor than cooler air. Thus,  $\Delta E$  shows remarkable  
509 high correlations at Medog and SETORS. At stations like Burang, Nyima, MAWORS, and Coqen,  
510 the most influential variable is soil moisture, followed by  $R_n$  and  $T_s$ . Thus, both energy and water  
511 availability play dominant roles. At extremely dry station of Mangai, most of the monthly  $LE$  values  
512 are close to zero, and none of the variations show obvious correlations with  $LE$ . For QOMOS, the  
513 largest correlation with  $LE$  is seen with soil moisture at 10 cm, suggesting that water availability  
514 plays a more critical role in  $ET$  than energy availability in this region.

515 In a brief summary, turbulent fluxes of  $SH$  and  $LE$  display clear spatial and seasonal patterns,  
516 with the Bowen ratio reflecting this energy partitioning. Correlation analyses reveal that  $SH$  is  
517 primarily driven by temperature gradients, whereas  $LE$  is controlled by energy-related factors in wet  
518 regions and by soil moisture availability in dry regions, highlighting the contrasting mechanisms of  
519 LA coupling across the TP.

### 520 **3.4 The seasonal variations of $NEE$ , $GPP$ and $Re$**

521 The seasonal variations of daily  $NEE$ ,  $GPP$ , and  $Re$ s averaged over the observational period  
522 show remarkable differences across sites, and the sites with relatively good vegetation coverage  
523 follow a single-peak distribution pattern, i.e. SETORS, Qamdo, Mangkam, etc., but the other sites,  
524 including Burang, Nyima, Coqen, Mangai, show weak or nearly non seasonal variations (Fig. 6 and  
525 Table 2). The carbon absorption and release are determined by vegetation photosynthesis process  
526 and ecosystem respiration. The seasonal variation of carbon fluxes follow the vegetation growth,  
527 with highest values during the summer peak growing seasons. For example, stations with substantial  
528 vegetation growth, such as SETORS, Qamdo, Mangkam, NADORS, and MAWORS, exhibit higher  
529 peaks and fluctuations in  $NEE$ ,  $GPP$ , and  $Re$ . The first three stations benefit from high precipitation,  
530 while the latter two stations receive considerable shallow soil water supply from surrounding lakes  
531 or glaciers. These five stations exhibit strong carbon sink capacities, with  $NEE$  values all smaller  
532 than  $-120 \text{ g C m}^{-2}$  during the growing season. Specifically, NADORS shows the largest  $NEE$  value  
533 of  $-174 \text{ g C m}^{-2}$  from May to October, while SETORS has the highest daily  $NEE$  values, exceeding  
534  $6 \text{ g C m}^{-2} \text{ d}^{-1}$ . Similarly,  $GPP$  and  $Re$  values at the 5 stations all exceed  $400 \text{ g C m}^{-2}$  and  $190 \text{ g C m}^{-2}$ ,  
535 with SETORS having the highest  $GPP$  and  $Re$  values of  $754 \text{ g C m}^{-2}$  and  $633 \text{ g C m}^{-2}$ , respectively,  
536 due to its favorable temperature and water conditions for vegetation growth. In water-limited regions  
537 like Mangai and Nyima, carbon fluxes fluctuations are minimal. Daily  $NEE$  values remain below  
538  $0.5 \text{ g C m}^{-2} \text{ d}^{-1}$ , even during the growing season. The total annual  $NEE$  values are  $-3.2 \text{ g C m}^{-2}$  and  
539  $-12.8 \text{ g C m}^{-2}$  in Mangai and Nyima, respectively.  $GPP$  and  $Re$  values are also low, with annual  
540 totals below  $70 \text{ g C m}^{-2}$  for  $GPP$  and  $40 \text{ g C m}^{-2}$  for  $Re$ . The smallest annual  $GPP$  value is  $56 \text{ g C}$   
541  $\text{m}^{-2}$  at Nyima, and the smallest annual  $Re$  value is  $20 \text{ g C m}^{-2}$  at Mangai. Although annual  $NEE$

542 values at SETORS and MAWORS are relatively similar, SETORS has much larger *GPP* and *Re*  
 543 values because of the efficient water supply and warm climate. In contrast, (Wang et al., 2021)  
 544 reported NADORS with average *GPP* value of  $1.60 \text{ g C m}^{-2} \text{ d}^{-1}$  and average *Re* value of  $0.71 \text{ g C}$   
 545  $\text{m}^{-2} \text{ d}^{-1}$  during growing season of 2014-2015, while these values ( $2.93 \text{ g C m}^{-2} \text{ d}^{-1}$  for *GPP* and  $1.35$   
 546  $\text{g C m}^{-2} \text{ d}^{-1}$  for *Re*) are much larger during growing season of 2021-2022 in our estimation. In addition,  
 547 the maximum net carbon uptake has a value of  $-2.1 \text{ g C m}^{-2} \text{ d}^{-1}$  in MAWORS during 2015-2016  
 548 (Wang et al., 2021), however, the largest *NEE* exchange value is  $-2.6 \text{ g C m}^{-2} \text{ d}^{-1}$  in our measurements.  
 549 Thus, it may indicate the improvement of vegetation status in the two western stations during the  
 550 past 10 years (Zhong et al., 2019b).



551  
 552 **Figure 6.** The seasonal variations in *NEE*, *GPP*, *Re* across different sites. The negative *NEE* values  
 553 indicated a net uptake of  $\text{CO}_2$ . The black, blue and red lines stand for daily *NEE*, *GPP* and *Re*,  
 554 respectively.

555 The annual *NEE* values are negative at 11 out of 12 stations, with exceptions at Medog (Table  
 556 1). The annual *NEE* values at the stations of Qamdo, SETORS, Mangkam, MAWORS and  
 557 NADORS all smaller than  $-120 \text{ g C}$ , coincident with stations with higher *ET* annual values,  
 558 suggesting the significance of water-carbon coupling in land-atmosphere interaction process. At  
 559 stations of Shuanghu, Burang, Jyirong, the annual *NEE* values are between  $-50 \text{ g C}$  and  $-100 \text{ g C}$   
 560 and the rest stations of Nyima and Mangai have annual *NEE* values of close to carbon neutral. At  
 561 Medog, despite substantial carbon absorption during the daytime, remarkable carbon release at night  
 562 caused by soil respiration leads to large carbon release. Mangai, with sparse vegetation, functions  
 563 nearly as carbon neutral. An obvious drastic variation of *NEE* values during August at Gyirong  
 564 station can be found and it corresponds to a soil drought event caused by water deficit. The water  
 565 deficit event results in decrease in *NEE* and *LE* and obvious increase in  $T_s$  and *SH*. Notably, carbon  
 566 absorption primarily occurs during summer growing seasons of May to September and function as  
 567 carbon neutral during winter seasons. The spatial distribution of annual *NEE* values generally follow

568 the distribution of water conditions, where sufficient water can promote vegetation growth, allowing  
569 photosynthesis to absorb more CO<sub>2</sub> than respiration releases (Wang et al., 2021; Wang et al., 2023).

570 Global forests have been widely recognized as carbon sinks (Hubau et al., 2020; Pan et al.,  
571 2024). Medog station, located in the Yarlung Zangbo River valley, is surrounded by subtropical  
572 forests and has an annual *NEE* value of 365 g C, indicating that the land cover acts as an obvious  
573 carbon source. Studies have indicated that tropical forests can become carbon sources due to factors  
574 such as deforestation, soil respiration exceeding photosynthesis, lingering droughts, and extreme  
575 warming (Gatti et al., 2021; Mills et al., 2023; Xie et al., 2016). During a severe drought in the  
576 summer of 2013 in a subtropical forest in China, the ecosystem switched to a net carbon source by  
577 late August (Xie et al., 2016). Mills et al. (2023) reported that tropical forests, following  
578 deforestation and degradation, can shift from carbon sinks to carbon sources. Similarly, the Medog  
579 station, located in a hot and humid region with complex terrain, has experienced recent site  
580 disturbance associated with station construction in the southern area, leading to partial vegetation  
581 removal and soil exposure. These disturbances likely enhanced soil and microbial respiration,  
582 resulting in net carbon release. Moreover, topographic shading caused by surrounding steep terrain  
583 reduces solar radiation exposure, thereby constraining photosynthesis (Wang et al., 2021; Wang et  
584 al., 2023). The pronounced seasonal variation in *GPP* at this site (Fig. 6) is mainly driven by  
585 monsoonal climatic conditions—*GPP* peaks during the warm and moist summer months when  
586 radiation and temperature are favorable but declines markedly during the cooler and cloudier pre-  
587 and post-monsoon periods (Fig. S6). Although *NEE* values can be obviously negative during the  
588 daytime due to photosynthesis, obvious and long-lasting ecosystem respiration at night leads to a  
589 net carbon release (Fig. S6).

590 Across the TP, carbon fluxes exhibit clear spatial and seasonal variability linked to vegetation  
591 cover and water availability. Stations with abundant precipitation or shallow groundwater act as  
592 strong carbon sinks, e.g. SETORS, NADORS, while arid sites such as Mangai and Nyima remain  
593 nearly carbon neutral. In contrast, the Medog station functions as a carbon source, likely due to  
594 vegetation disturbance, soil respiration, and complex topographic and climatic conditions that limit  
595 photosynthetic uptake.

## 596 **4 Conclusions**

597 The establishment of a comprehensive observation and research platform marks a remarkable  
598 advancement in understanding land-atmosphere water, heat and CO<sub>2</sub> flux across diverse stations.  
599 The platform features standardized configurations at each station, including an EC system, a 20 m  
600 PBL tower measuring wind, temperature, and humidity across five layers, soil moisture and  
601 temperature probes at five depths, energy budget probes for radiation components and soil heat flux,  
602 a thermal infrared temperature probe, a barometer, and a rain gauge. It covers a range of landscapes  
603 such as alpine steppe, alpine meadow, grassland, bare ground, forest, and desert. The observation  
604 platform aims to provide long-term, standardized, high-quality data on land-atmosphere interaction  
605 processes over the TP, with a particular focus on the data-scarce regions of the western TP. The  
606 extensive hydrometeorological dataset offers initial insights into the spatial and temporal variations  
607 of meteorological conditions, liquid precipitation, and turbulent fluxes. Diurnal precipitation

608 patterns reveal three types: peak at night, peak during the day, and bimodal peaks. While liquid  
609 precipitation can distinguish between water-limited and energy-limited regions, soil moisture—both  
610 from surface and deeper layers—also plays a key role in *ET*, as seen in stations like NADORS and  
611 Shuanghu. *NEE* fluxes are near zero at bare ground stations, show notable carbon release in forested  
612 areas under construction, and function as carbon sinks in most alpine meadows and alpine steppe  
613 sites. This platform is critical for supporting scientific research and sustainable development.  
614 However, challenges remain in capturing data from remote and heterogeneous regions, as well as  
615 limitations in current technologies. Scaling flux towers for global models remains difficult,  
616 highlighting the need for robust interpolation and validation techniques. Additionally, further  
617 investigation is required to understand the impacts of land-use changes, such as deforestation and  
618 reforestation, on turbulent heat fluxes and their feedback to the climate system.

## 619 **Competing interests**

620 The authors declare that they have no conflict of interest.

## 621 **Author contribution**

622 BBW and YMM jointly led the writing of this article and were responsible for the establishment  
623 and maintenance of the experimental sites and instrumentation. BBW took the lead in dataset  
624 consolidation, processed the data into the standardized format described in this study, and drafted  
625 the manuscript in collaboration with all co-authors. ZYH, XL, WQM, XLC, CBH, ZPX, YYW,  
626 MSL, BM, XDS, WML, and ZLC contributed to the maintenance of the observation systems, data  
627 analysis, and provided critical feedback and revisions to the manuscript.

## 628 **Data availability statement**

629 The hourly dataset including air temperature, air humidity, wind speed, land surface  
630 temperature, soil moisture, downward shortwave radiation, downward longwave radiation, upward  
631 shortwave radiation, upward longwave radiation, sensible heat flux, latent heat flux, Net ecosystem  
632 change can be downloaded freely in the Tibetan Plateau Data Center. The DOI of the dataset is  
633 <https://doi.org/10.11888/Atmos.tpd.302428>. The data can be referenced by Wang and Ma (2025).  
634 The web link is <https://data.tpd.ac.cn/en/disallow/e8032ff8-2437-4363-876f-2af4e4558a4d>. New  
635 collected data will be properly processed and added to this web link in the Tibetan Plateau Data  
636 Center.

## 637 **Acknowledgement**

638 This research was jointly funded by the National Key Research and Development Program of  
639 China (2023YFF0805300), the National Natural Science Foundation of China (Grant Nos.  
640 U2442213 and 42230610), the Youth Innovation Promotion Association of the Chinese Academy  
641 of Sciences (Grant No. 2022069), the Second Tibetan Plateau Scientific Expedition and Research  
642 Program (Grant No. 2019QZKK0103).

## 643 **References**

644 André, J. C., Goutorbe, J. P., and Perrier, A.: HAPEX—MOBILHY: A Hydrologic Atmospheric  
645 Experiment the Study of Water Budget and Evaporation Flux at the Climatic Scale, *Bulletin of the*

646 *American Meteorological Society*, 67(2), 138-144, doi:<https://doi.org/10.1175/1520-0477-67.2.138>,  
647 1986.

648 Baldocchi, D.: Measuring fluxes of trace gases and energy between ecosystems and the atmosphere – the  
649 state and future of the eddy covariance method, *Global Change Biology*, 20(12), 3600-3609,  
650 doi:<https://doi.org/10.1111/gcb.12649>, 2014.

651 Bei, N., Zhao, L., Wu, J., Li, X., Feng, T., and Li, G.: Impacts of sea-land and mountain-valley  
652 circulations on the air pollution in Beijing-Tianjin-Hebei (BTH): A case study, *Environmental Pollution*,  
653 234, 429-438, doi:<https://doi.org/10.1016/j.envpol.2017.11.066>, 2018.

654 Chen, X., Cao, D., Liu, Y., Xu, X., and Ma, Y.: An observational view of rainfall characteristics and  
655 evaluation of ERA5 diurnal cycle in the Yarlung Tsangbo Grand Canyon, China, *Quarterly Journal of*  
656 *the Royal Meteorological Society*, 149(753), 1459-1472, doi:<https://doi.org/10.1002/qj.4468>, 2023.

657 Duan, A., and Xiao, Z.: Does the climate warming hiatus exist over the Tibetan Plateau?, *Scientific*  
658 *Reports*, 5(1), 13711, doi:10.1038/srep13711, 2015.

659 Foken, T.: THE ENERGY BALANCE CLOSURE PROBLEM: AN OVERVIEW, *Ecological*  
660 *Applications*, 18(6), 1351-1367, doi:<https://doi.org/10.1890/06-0922.1>, 2008.

661 Friedlingstein, P., O'Sullivan, M., Jones, M. W., Andrew, R. M., Gregor, L., Hauck, J., Le Quéré, C.,  
662 Lujikx, I. T., Olsen, A., Peters, G. P., Peters, W., Pongratz, J., Schwingshackl, C., Sitch, S., Canadell, J.  
663 G., Ciais, P., Jackson, R. B., Alin, S. R., Alkama, R., Arneeth, A., Arora, V. K., Bates, N. R., Becker, M.,  
664 Bellouin, N., Bittig, H. C., Bopp, L., Chevallier, F., Chini, L. P., Cronin, M., Evans, W., Falk, S., Feely,  
665 R. A., Gasser, T., Gehlen, M., Gkritzalis, T., Gloege, L., Grassi, G., Gruber, N., Gürses, Ö., Harris, I.,  
666 Hefner, M., Houghton, R. A., Hurtt, G. C., Iida, Y., Ilyina, T., Jain, A. K., Jersild, A., Kadono, K., Kato,  
667 E., Kennedy, D., Klein Goldewijk, K., Knauer, J., Korsbakken, J. I., Landschützer, P., Lefèvre, N.,  
668 Lindsay, K., Liu, J., Liu, Z., Marland, G., Mayot, N., McGrath, M. J., Metzl, N., Monacci, N. M., Munro,  
669 D. R., Nakaoka, S.-I., Niwa, Y., O'Brien, K., Ono, T., Palmer, P. I., Pan, N., Pierrot, D., Pockock, K.,  
670 Poulter, B., Resplandy, L., Robertson, E., Rödenbeck, C., Rodriguez, C., Rosan, T. M., Schwinger, J.,  
671 Séférian, R., Shutler, J. D., Skjelvan, I., Steinhoff, T., Sun, Q., Sutton, A. J., Sweeney, C., Takao, S.,  
672 Tanhua, T., Tans, P. P., Tian, X., Tian, H., Tilbrook, B., Tsujino, H., Tubiello, F., van der Werf, G. R.,  
673 Walker, A. P., Wanninkhof, R., Whitehead, C., Willstrand Wranne, A., Wright, R., Yuan, W., Yue, C., Yue,  
674 X., Zaehle, S., Zeng, J., and Zheng, B.: Global Carbon Budget 2022, *Earth Syst. Sci. Data*, 14, 4811–  
675 4900, <https://doi.org/10.5194/essd-14-4811-2022>, 2022.

676 Gatti, Luciana V., Luana S. Basso, John B. Miller, Manuel Gloor, Lucas Gatti Domingues, Henrique L.  
677 G. Cassol, Graciela Tejada, Luiz E. O. C. Aragão, Carlos Nobre, Wouter Peters, Luciano Marani, Egidio  
678 Arai, Alber H. Sanches, Sergio M. Corrêa, Liana Anderson, Celso Von Randow, Caio S. C. Correia,  
679 Stephane P. Crispim, and Raiane A. L. Neves.: Amazonia as a carbon source linked to deforestation and  
680 climate change. *Nature* 595, 388–393, <https://doi.org/10.1038/s41586-021-03629-6>, 2021.

681 Gentine, P., Massmann, A., Lintner, B. R., Hamed Alemohammad, S., Fu, R., Green, J. K., Kennedy, D.,  
682 and Vilà-Guerau de Arellano, J.: Land–atmosphere interactions in the tropics – a review, *Hydrol. Earth*  
683 *Syst. Sci.*, 23, 4171–4197, <https://doi.org/10.5194/hess-23-4171-2019>, 2019.

684 Gerken, T., Biermann, T., Babel, W., Herzog, M., Ma, Y., Foken, T., and Graf, H. F.: A modelling  
685 investigation into lake-breeze development and convection triggering in the Nam Co Lake basin, Tibetan  
686 Plateau, *Theoretical and Applied Climatology*, 117(1), 149-167, doi:10.1007/s00704-013-0987-9, 2014.

687 Goutorbe, J. P., Lebel, T., Dolman, A.J., Gash, J.H.C., Kabat, P., Kerr, Y.H., Monteny, B., Prince, S.D.,  
688 Stricker, J.N.M., Tinga, A., Wallace, J.S.: An overview of HAPEX-Sahel: a study in climate and

689 desertification, *Journal of Hydrology*, 188-189, 4-17, doi:[https://doi.org/10.1016/S0022-1694\(96\)03308-](https://doi.org/10.1016/S0022-1694(96)03308-2)  
690 [2](https://doi.org/10.1016/S0022-1694(96)03308-2), 1997.

691 Halldin, S., Gryning, S. E., Gottschalk, L., Jochum, A., Lundin, L. C., and Van de Griend, A. A.: Energy,  
692 water and carbon exchange in a boreal forest landscape — NOPEX experiences, *Agricultural and Forest*  
693 *Meteorology*, 98-99, 5-29, doi:[https://doi.org/10.1016/S0168-1923\(99\)00148-3](https://doi.org/10.1016/S0168-1923(99)00148-3), 1999.

694 Huang, J., Zhou, X., Wu, G., Xu, X., Zhao, Q., Liu, Y., Duan, A., Xie, Y., Ma, Y., Zhao, P., Yang, S., Yang,  
695 K., Yang, H., Bian, J., Fu, Y., Ge, J., Liu, Y., Wu, Q., Yu, H., Wang, B., Bao, Q., and Qie, K.: Global  
696 Climate Impacts of Land-Surface and Atmospheric Processes Over the Tibetan Plateau, *Reviews of*  
697 *Geophysics*, 61(3), e2022RG000771, doi:<https://doi.org/10.1029/2022RG000771>, 2023.

698 Hubau, W., Lewis, S. L., Phillips, O. L., Affum-Baffoe, K., Beeckman, H., Cuní-Sanchez, A., Daniels,  
699 A. K., Ewango, C. E. N., Fauset, S., Mukinzi, J. M., Sheil, D., Sonké, B., Sullivan, M. J. P., Sunderland,  
700 T. C. H., Taedoumg, H., Thomas, S. C., White, L. J. T., Abernethy, K. A., Adu-Bredu, S., Amani, C. A.,  
701 Baker, T. R., Banin, L. F., Baya, F., Begne, S. K., Bennett, A. C., Benedet, F., Bitariho, R., Bocko, Y. E.,  
702 Boeckx, P., Boundja, P., Brienen, R. J. W., Brncic, T., Chezeaux, E., Chuyong, G. B., Clark, C. J., Collins,  
703 M., Comiskey, J. A., Coomes, D. A., Dargie, G. C., de Haulleville, T., Djuikouo Kamdem, M. N., Doucet,  
704 J. L., Esquivel-Muelbert, A., Feldpausch, T. R., Fofanah, A., Foli, E. G., Gilpin, M., Gloor, E., Gonmadje,  
705 C., Gourlet-Fleury, S., Hall, J. S., Hamilton, A. C., Harris, D. J., Hart, T. B., Hockemba, M. B. N., Hladik,  
706 A., Ifo, S. A., Jeffery, K. J., Jucker, T., Yakusu, E. K., Kearsley, E., Kenfack, D., Koch, A., Leal, M. E.,  
707 Levesley, A., Lindsell, J. A., Lisingo, J., Lopez-Gonzalez, G., Lovett, J. C., Makana, J. R., Malhi, Y.,  
708 Marshall, A. R., Martin, J., Martin, E. H., Mbayu, F. M., Medjibe, V. P., Mihindou, V., Mitchard, E. T.  
709 A., Moore, S., Munishi, P. K. T., Bengone, N. N., Ojo, L., Ondo, F. E., Peh, K. S. H., Pickavance, G. C.,  
710 Poulsen, A. D., Poulsen, J. R., Qie, L., Reitsma, J., Rovero, F., Swaine, M. D., Talbot, J., Taplin, J., Taylor,  
711 D. M., Thomas, D. W., Toirambe, B., Mukendi, J. T., Tuagben, D., Umunay, P. M., van der Heijden, G.  
712 M. F., Verbeeck, H., Vleminckx, J., Willcock, S., Wöll, H., Woods, J. T., and Zemagho, L.: Asynchronous  
713 carbon sink saturation in African and Amazonian tropical forests, *Nature*, 579(7797), 80-87,  
714 doi:10.1038/s41586-020-2035-0, 2020.

715 Li, G., Yu, Z., Wang, W., Ju, Q., and Chen, X.: Analysis of the spatial Distribution of precipitation and  
716 topography with GPM data in the Tibetan Plateau, *Atmospheric Research*, 247, 105259,  
717 <https://doi.org/10.1016/j.atmosres.2020.105259>, 2021a.

718 Li, L., Zhang, R., Wu, P., Wen, M., and Duan, J.: Roles of Tibetan Plateau vortices in the heavy rainfall  
719 over southwestern China in early July 2018, *Atmospheric Research*, 245, 105059,  
720 <https://doi.org/10.1016/j.atmosres.2020.105059>, 2020

721 Li, P., Furtado, K., Zhou, T., Chen, H., and Li, J.: Convection-permitting modelling improves simulated  
722 precipitation over the central and eastern Tibetan Plateau, *Quarterly Journal of the Royal Meteorological*  
723 *Society*, 147(734), 341-362, <https://doi.org/10.1002/qj.3921>, 2021b

724 Liu, S., Li, X., Xu, Z., Che, T., Xiao, Q., Ma, M., Liu, Q., Jin, R., Guo, J., Wang, L., Wang, W., Qi, Y.,  
725 Li, H., Xu, T., Ran, Y., Hu, X., Shi, S., Zhu, Z., Tan, J., Zhang, Y., and Ren, Z.: The Heihe Integrated  
726 Observatory Network: A Basin-Scale Land Surface Processes Observatory in China, *Vadose Zone*  
727 *Journal*, 17(1), 180072, <https://doi.org/10.2136/vzj2018.04.0072>, 2018.

728 Lü, D., Chen, Z., Wang, G., Chen, J., Ji, J., Li, Y., and Chen, H.: Inner Mongolia Semi-Arid Grassland  
729 Soil-Vegetation-Atmosphere Interaction, *Climatic and Environmental Research*, 2(3), 199-209,  
730 doi:10.3878/j.issn.1006-9585.1997.03.01, 1997.

731 Ma, N., and Zhang, Y.: Increasing Tibetan Plateau terrestrial evapotranspiration primarily driven by  
732 precipitation, *Agricultural and Forest Meteorology*, 317, 108887,  
733 <https://doi.org/10.1016/j.agrformet.2022.108887>, 2022.

734 Ma, Y., Fan, S., Ishikawa, H., Tsukamoto, O., Yao, T., Koike, T., Zuo, H., Hu, Z., and Su, Z.: Diurnal and  
735 inter-monthly variation of land surface heat fluxes over the central Tibetan Plateau area, *Theoretical and*  
736 *Applied Climatology*, 80(2), 259-273, doi:10.1007/s00704-004-0104-1, 2005.

737 Ma, Y., Hu, Z., Xie, Z., Ma, W., Wang, B., Chen, X., Li, M., Zhong, L., Sun, F., Gu, L., Han, C., Zhang,  
738 L., Liu, X., Ding, Z., Sun, G., Wang, S., Wang, Y., and Wang, Z.: A long-term (2005–2016) dataset of  
739 hourly integrated land–atmosphere interaction observations on the Tibetan Plateau, *Earth Syst. Sci. Data*,  
740 12(4), 2937-2957, doi:10.5194/essd-12-2937-2020, 2020.

741 Ma, Y., Wang, Y., and Han, C.: Regionalization of land surface heat fluxes over the heterogeneous  
742 landscape: from the Tibetan Plateau to the Third Pole region, *International Journal of Remote Sensing*,  
743 39(18), 5872-5890, doi:10.1080/01431161.2018.1508923, 2018.

744 Ma, Y., Xie, Z., Chen, Y., Liu, S., Che, T., Xu, Z., Shang, L., He, X., Meng, X., Ma, W., Xu, B., Zhao,  
745 H., Wang, J., Wu, G., and Li, X.: Dataset of spatially extensive long-term quality-assured land–  
746 atmosphere interactions over the Tibetan Plateau, *Earth Syst. Sci. Data*, 16(6), 3017-3043,  
747 doi:10.5194/essd-16-3017-2024, 2024.

748 Ma, Y., Yao, T., Zhong, L., Wang, B., Xu, X., Hu, Z., Ma, W., Sun, F., Han, C., Li, M., Chen, X., Wang,  
749 J., Li, Y., Gu, L., Xie, Z., Liu, L., Sun, G., Wang, S., Zhou, D., Zuo, H., and Wang, Z.: Comprehensive  
750 study of energy and water exchange over the Tibetan Plateau: A review and perspective: From  
751 GAME/Tibet and CAMP/Tibet to TORP, TPEORP, and TPEITORP, *Earth-Science Reviews*, 237, 104312,  
752 <https://doi.org/10.1016/j.earscirev.2023.104312>, 2023.

753 Ma, Y., Kang, S., Zhu, L., Xu, B., Tian, L., and Yao, T.: TIBETAN OBSERVATION AND RESEARCH  
754 PLATFORM Atmosphere-Land Interaction over a Heterogeneous Landscape, *Bulletin of the American*  
755 *Meteorological Society*, 89(10), 1487-1492, 2008.

756 Massman, W. J., and Lee, X.: Eddy covariance flux corrections and uncertainties in long-term studies of  
757 carbon and energy exchanges, *Agricultural and Forest Meteorology*, 113(1), 121-144,  
758 [https://doi.org/10.1016/S0168-1923\(02\)00105-3](https://doi.org/10.1016/S0168-1923(02)00105-3), 2002.

759 Mauder, M., Cuntz, M., Drüe, C., Graf, A., Rebmann, C., Schmid, H. P., Schmidt, M., and Steinbrecher,  
760 R.: A strategy for quality and uncertainty assessment of long-term eddy-covariance measurements,  
761 *Agricultural and Forest Meteorology*, 169, 122-135, <https://doi.org/10.1016/j.agrformet.2012.09.006>,  
762 2013.

763 Mauder, M., and Foken, T.: Impact of post-field data processing on eddy covariance flux estimates and  
764 energy balance closure, *Meteorologische Zeitschrift*, 15(6), 597-609, doi:10.1127/0941-2948/2006/0167,  
765 2006.

766 Mauder, M., Foken, T., and Cuxart, J.: Surface-Energy-Balance Closure over Land: A Review, *Boundary-*  
767 *Layer Meteorology*, 177(2), 395-426, doi:10.1007/s10546-020-00529-6, 2020.

768 Mills, M. B., Malhi, Y., Ewers, R. M., Kho, L. K., Teh, Y. A., Both, S., Burslem, D. F. R. P., Majalap, N.,  
769 Nilus, R., Huasco, W. H., Cruz, R., Pillco, M. M., Turner, E. C., Reynolds, G., and Riutta, T.: Tropical  
770 forests post-logging are a persistent net carbon source to the atmosphere, *Proceedings of the National*  
771 *Academy of Sciences*, 120(3), e2214462120, doi:10.1073/pnas.2214462120, 2023.

772 Oku, Y., Ishikawa, H., Haginoya, S., and Ma, Y.: Recent Trends in Land Surface Temperature on the  
773 Tibetan Plateau, *Journal of Climate*, 19(12), 2995-3003, <https://doi.org/10.1175/JCLI3811.1>, 2006.

774 Pan, Y., Birdsey, R. A., Phillips, O. L., Houghton, R. A., Fang, J., Kauppi, P. E., Keith, H., Kurz, W. A.,

775 Ito, A., Lewis, S. L., Nabuurs, G. J., Shvidenko, A., Hashimoto, S., Lerink, B., Schepaschenko, D.,  
776 Castanho, A., and Murdiyarso, D.: The enduring world forest carbon sink. *Nature* 631, 563–569,  
777 <https://doi.org/10.1038/s41586-024-07602-x> , 2024.

778 Qi, Y., Wei, D., Zhao, H., and Wang, X.: Carbon Sink of a Very High Marshland on the Tibetan Plateau,  
779 *Journal of Geophysical Research: Biogeosciences*, 126(4), e2020JG006235,  
780 <https://doi.org/10.1029/2020JG006235>, 2021.

781 Santanello Jr., J. A., Dirmeyer, P. A., Ferguson, C. R., Findell, K. L., Tawfik, A. B., Berg, A., Ek, M.,  
782 Gentine, P., Guillod, B. P., van Heerwaarden, C., Roundy, J., and Wulfmeyer, V.: Land–Atmosphere  
783 Interactions: The LoCo Perspective, *Bulletin of the American Meteorological Society*, 99(6), 1253-1272,  
784 <https://doi.org/10.1175/BAMS-D-17-0001.1>, 2018.

785 Sellers, P., Hall, F., Margolis, H., Kelly, B., Baldocchi, D., den Hartog, G., Cihlar, J., Ryan, M. G.,  
786 Goodison, B., Crill, P., Ranson, K. J., Lettenmaier, D., and Wickland, D. E.: The Boreal Ecosystem–  
787 Atmosphere Study (BOREAS): An Overview and Early Results from the 1994 Field Year, *Bulletin of the*  
788 *American Meteorological Society*, 76(9), 1549-1577, [https://doi.org/10.1175/1520-0477\(1995\)076<1549:TBESAO>2.0.CO;2](https://doi.org/10.1175/1520-0477(1995)076<1549:TBESAO>2.0.CO;2), 1995.

790 Sellers, P. J., Hall, F. G., Asrar, G., Strelbel, D. E., and Murphy, R. E.: An overview of the First  
791 International Satellite Land Surface Climatology Project (ISLSCP) Field Experiment (FIFE), *Journal of*  
792 *Geophysical Research: Atmospheres*, 97(D17), 18345-18371, <https://doi.org/10.1029/92JD02111>, 1992.

793 Seo, Y.-W., and Ha, K.-J.: Changes in land-atmosphere coupling increase compound drought and  
794 heatwaves over northern East Asia, *npj Climate and Atmospheric Science*, 5(1), 100,  
795 doi:10.1038/s41612-022-00325-8, 2022.

796 Suni, T., Guenther, A., Hansson, H. C., Kulmala, M., Andreae, M. O., Arneth, A., Artaxo, P., Blyth, E.,  
797 Brus, M., Ganzeveld, L., Kabat, P., de Noblet-Ducoudré, N., Reichstein, M., Reissell, A., Rosenfeld, D.,  
798 and Seneviratne, S.: The significance of land-atmosphere interactions in the Earth system—iLEAPS  
799 achievements and perspectives, *Anthropocene*, 12, 69-84, <https://doi.org/10.1016/j.ancene.2015.12.001>,  
800 2015.

801 Turetsky, M. R., Abbott, B. W., Jones, M. C., Anthony, K. W., Olefeldt, D., Schuur, E. A. G., Grosse, G.,  
802 Kuhry, P., Hugelius, G., Koven, C., Lawrence, D. M., Gibson, C., Sannel, A. B. K., and McGuire, A. D.:  
803 Carbon release through abrupt permafrost thaw, *Nature Geoscience*, 13(2), 138-143,  
804 doi:10.1038/s41561-019-0526-0, 2020.

805 Twine, T. E., Kustas, W. P., Norman, J. M., Cook, D. R., Houser, P. R., Meyers, T. P., Prueger, J. H.,  
806 Starks, P. J., and Wesely, M. L.: Correcting eddy-covariance flux underestimates over a grassland,  
807 *Agricultural and Forest Meteorology*, 103(3), 279-300, [https://doi.org/10.1016/S0168-1923\(00\)00123-](https://doi.org/10.1016/S0168-1923(00)00123-4)  
808 [4](https://doi.org/10.1016/S0168-1923(00)00123-4), 2000.

809 Wang, S., and Ma, Y.: Characteristics of Land-Atmosphere Interaction Parameters over the Tibetan  
810 Plateau, *Journal of Hydrometeorology*, 12(4), 702–708, <https://doi.org/10.1175/2010JHM1275.1>, 2011.

811 Wang, B., Ma, Y., Ma, W., and Su, Z.: Physical controls on half-hourly, daily, and monthly turbulent flux  
812 and energy budget over a high-altitude small lake on the Tibetan Plateau, *Journal of Geophysical*  
813 *Research: Atmospheres*, 122(4), 2289-2303, <https://doi.org/10.1002/2016JD026109>, 2017.

814 Wang, B., Ma, Y.: Meteorological variables and eddy fluxes at 15 land-atmosphere interaction stations  
815 over the Tibetan Plateau (May-2021 to July 2023). National Tibetan Plateau / Third Pole Environment  
816 Data Center. <https://doi.org/10.11888/Atmos.tpcd.302428>, 2025.

817 Wang, Y., Xiao, J., Ma, Y., Ding, J., Chen, X., Ding, Z., and Luo, Y.: Persistent and enhanced carbon  
818 sequestration capacity of alpine grasslands on Earth's Third Pole, *Science Advances*, *9*(20),  
819 doi:10.1126/sciadv.ade6875, 2023.

820 Wang, Y., Xiao, J., Ma, Y., Luo, Y., Hu, Z., Li, F., Li, Y., Gu, L., Li, Z., and Yuan, L.: Carbon fluxes and  
821 environmental controls across different alpine grassland types on the Tibetan Plateau, *Agricultural and  
822 Forest Meteorology*, *311*, 108694, <https://doi.org/10.1016/j.agrformet.2021.108694>, 2021.

823 Wei, D., Qi, Y., Ma, Y., Wang, X., Ma, W., Gao, T., Huang, L., Zhao, H., Zhang, J., and Wang, X.: Plant  
824 uptake of CO<sub>2</sub> outpaces losses from permafrost and plant respiration on the Tibetan Plateau,  
825 *Proceedings of the National Academy of Sciences*, *118*(33), e2015283118, doi:10.1073/pnas.2015283118,  
826 2021.

827 Wilson, K., Goldstein, A., Falge, E., Aubinet, M., Baldocchi, D., Berbigier, P., Bernhofer, C., Ceulemans,  
828 R., Dolman, H., Field, C., Grelle, A., Ibrom, A., Law, B. E., Kowalski, A., Meyers, T., Moncrieff, J.,  
829 Monson, R., Oechel, W., Tenhunen, J., Valentini, R., and Verma, S.: Energy balance closure at FLUXNET  
830 sites, *Agricultural and Forest Meteorology*, *113*(1), 223-243, [https://doi.org/10.1016/S0168-  
831 1923\(02\)00109-0](https://doi.org/10.1016/S0168-831), 2002.

832 Wu, G., and Zhang, Y.: Tibetan Plateau Forcing and the Timing of the Monsoon Onset over South Asia  
833 and the South China Sea, *Monthly Weather Review*, *126*(4), 913-927, [https://doi.org/10.1175/1520-  
834 0493\(1998\)126<0913:TPFATT>2.0.CO;2](https://doi.org/10.1175/1520-834), 1998.

835 Wu, G., Zhou, X., Xu, X., Huang, J., Duan, A., Yang, S., Hu, W., Ma, Y., Liu, Y., Bian, J., Fu, Y., Yang,  
836 H., Zhao, P., Zhong, L., and Ma, W.: An Integrated Research Plan for the Tibetan Plateau Land–Air  
837 Coupled System and Its Impacts on the Global Climate, *Bulletin of the American Meteorological Society*,  
838 *104*(1), E158-E177, <https://doi.org/10.1175/BAMS-D-21-0293.1>, 2023.

839 Wutzler, T., Lucas-Moffat, A., Migliavacca, M., Knauer, J., Sickel, K., Šigut, L., Menzer, O., and  
840 Reichstein, M.: Basic and extensible post-processing of eddy covariance flux data with REddyProc,  
841 *Biogeosciences*, *15*(16), 5015-5030, doi:10.5194/bg-15-5015-2018, 2018.

842 Xie, Z., Wang, L., Jia, B., and Yuan, X.: Measuring and modeling the impact of a severe drought on  
843 terrestrial ecosystem CO<sub>2</sub> and water fluxes in a subtropical forest, *Journal of Geophysical Research:  
844 Biogeosciences*, *121*(10), 2576-2587, <https://doi.org/10.1002/2016JG003437>, 2016.

845 Xu, X., and Chen, L.: Advances of the Study on Tibetan Plateau Experiment of Atmospheric Sciences,  
846 *Journal of Applied Meteorological Science*, *17*(6), 756-772, 2016.

847 Yang, K., Chen, Y., Lazhu, Zhan, C., Ling, X., Zhou, X., Jiang, Y., Yao, X., Lu, H., Ma, X., Ouyang, L.,  
848 Pan, W., Ren, Y., Shao, C., Tian, J., Wang, Y., Yang, H., Yue, S., Zhang, K., Zhao, D., Zhao, L., Zhou, J.,  
849 and Zou, M.: Cross-sectional rainfall observation on the central-western Tibetan Plateau in the warm  
850 season: System design and preliminary results, *Science China Earth Sciences*, *66*(5), 1015-1030,  
851 doi:10.1007/s11430-022-1081-4, 2023.

852 Yang, K., Koike, T., Ishikawa, H., Kim, J., Li, X., Liu, H., Liu, S., Ma, Y., and Wang, J.: Turbulent Flux  
853 Transfer over Bare-Soil Surfaces: Characteristics and Parameterization, *Journal of Applied Meteorology  
854 and Climatology*, *47*(1), 276–290, <https://doi.org/10.1175/2007JAMC1547.1>, 2008.

855 Yao, N., Ma, Y., Wang, B., Zou, J., Sun, J., and Xie, Z.: A comparative study of the land–atmosphere  
856 energy and water exchanges over the Tibetan Plateau and the Yangtze River Region, *Atmospheric and  
857 Oceanic Science Letters*, *17*(2), 100447, <https://doi.org/10.1016/j.aosl.2023.100447>, 2024.

858 Ye, D., and Wu, G.: The role of the heat source of the Tibetan Plateau in the general circulation,  
859 *Meteorology and Atmospheric Physics*, *67*(1), 181-198, <https://doi.org/10.1007/BF01277509>, 1998.

860 Yu, G., Chen, Z., and Wang, Y.: Carbon, water and energy fluxes of terrestrial ecosystems in China,  
861 *Agricultural and Forest Meteorology*, 346, 109890, <https://doi.org/10.1016/j.agrformet.2024.109890>,  
862 2024.

863 Yuan, L., Chen, X., Ma, Y., Han, C., Wang, B., and Ma, W.: Long-term monthly 0.05° terrestrial  
864 evapotranspiration dataset (1982–2018) for the Tibetan Plateau, *Earth Syst. Sci. Data*, 16(2), 775-801,  
865 doi:10.5194/essd-16-775-2024, 2024.

866 Yuan, L., Ma, Y., Chen, X., Wang, Y., and Li, Z.: An Enhanced MOD16 Evapotranspiration Model for  
867 the Tibetan Plateau During the Unfrozen Season, *Journal of Geophysical Research: Atmospheres*, 126,  
868 <https://doi.org/10.1029/2020JD032787>, 2021.

869 Zhang, C., Qin, D.-H., and Zhai, P.-M.: Amplification of warming on the Tibetan Plateau, *Advances in*  
870 *Climate Change Research*, 14(4), 493-501, <https://doi.org/10.1016/j.accre.2023.07.004>, 2023.

871 Zhang, Y., Wagner, N., Goergen, K., and Kollet, S.: Summer evapotranspiration-cloud feedbacks in land-  
872 atmosphere interactions over Europe *Climate Dynamics*, 62, 10767–10783,  
873 <https://doi.org/10.1007/s00382-024-07475-w>, 2024.

874 Zhao, L., Li, Y., Zhao, X., Xu, S., Tang, Y., Yu, G., Gu, S., Du, M., and Wang, Q.: Comparative study of  
875 the net exchange of CO<sub>2</sub> in 3 types of vegetation ecosystems on the Qinghai-Tibetan Plateau, *Chinese*  
876 *Science Bulletin*, 50(16), 1767-1774, <https://doi.org/10.1360/04wd0316>, 2005.

877 Zhong, L., Ma, Y., Hu, Z., Fu, Y., Hu, Y., Wang, X., Cheng, M., and Ge, N.: Estimation of hourly land  
878 surface heat fluxes over the Tibetan Plateau by the combined use of geostationary and polar-orbiting  
879 satellites, *Atmos. Chem. Phys*, 19(8), 5529-5541, <https://doi.org/10.5194/acp-19-5529-2019>, 2019.

880 Zhu, L., Meng, Z., Zhang, F., and Markowski, P. M.: The influence of sea- and land-breeze circulations  
881 on the diurnal variability in precipitation over a tropical island, *Atmos. Chem. Phys*, 17(21), 13213-13232,  
882 <https://doi.org/10.5194/acp-17-13213-2017>, 2017.